

Univ.Prof. Friedrich Aumayr



**TECHNISCHE
UNIVERSITÄT
WIEN**

Vienna University of Technology

DIPLOMARBEIT

Search for experimental evidence of mode coupling during the ELM cycle from magnetic measurements in ASDEX Upgrade

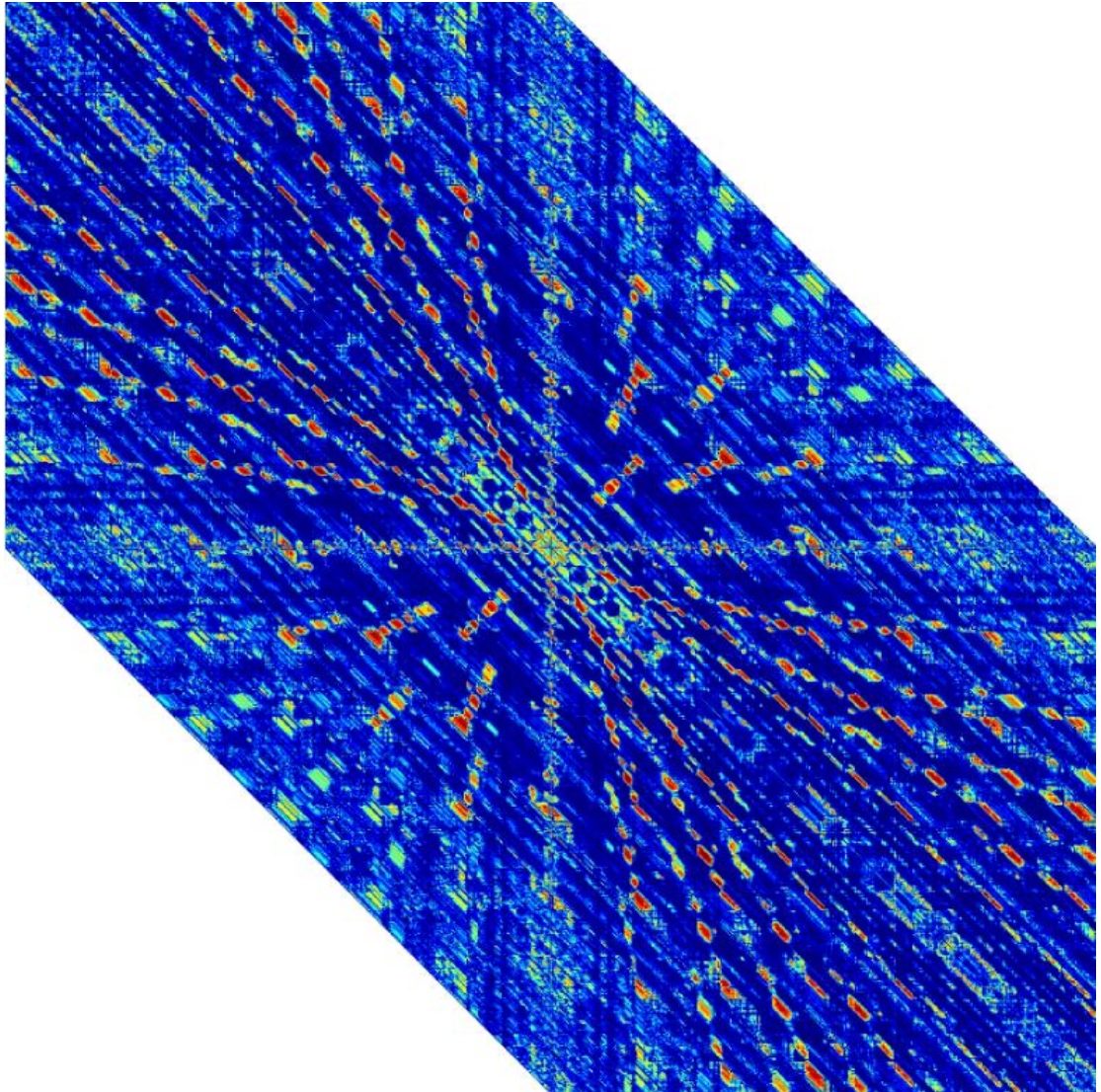
Ausgeführt am
Institut für Angewandte Physik
der Technischen Universität Wien
und am
Max-Planck-Institut für Plasmaphysik
in Garching

unter der Anleitung von
Univ.Prof. Dr. Friedrich Aumayr
Univ.Do. Dr. Elisabeth Wolfrum
Dr. Peter Manz
Felician Mink, M.Sc.

durch
Georg Harrer
Matrikelnummer 0927542 Kennzahl 066 461
Winterzeile 116, A-2091 Langau

Wien, October 30, 2016

Georg Harrer



Abstract

The foreseen operation scenario for future fusion devices like ITER and DEMO is the high confinement mode (H-mode), which is characterized by high pressure and current density gradients in the plasma edge due to an edge transport barrier (ETB). These steep gradients provide a source of free energy for magnetohydrodynamic instabilities. One property of the H-mode are the quasi periodically occurring edge localized modes (ELMs), which lead to the degradation of the ETB. The best model so far, which describes the critical quantities driving the ELM unstable, is the peeling-ballooning model, in which peeling modes, driven by the current density and its gradients, as well as ballooning modes, driven by the pressure gradients, combine to form peeling-ballooning modes.

This Master Thesis deals with non-linear coupling of magnetic modes in ASDEX Upgrade plasma discharges. A theoretical model first shows how coupling of modes in waves, and therefore also in plasma fluctuations, develops. Bicoherence analysis delivers a method to diagnose and dispaly these couplings. Over the course of this thesis a bicoherence algorithm was developed and thoroughly tested. Windowing and dithering turned out to be useful tools to decrease the noise sensitivity and increase the stability of the algorithm.

To test the capabilities of the algorithm in analyzing experimental data, signals of magnetic pick-up coils from different AUG discharges were analyzed and displayed. The magnetic signals were then synchronized to the ELM onsets to check for coupling before, during and after the ELMs. This method preserves the important properties of the ELMs while removing unimportant ones. Consequently these ELM synchronized signals were divided into distinct phases and separatly analyzed with the bicoherence algorithm. No apparent mode couplings were found in any of the ELM phases.

Kurzfassung

Zukünftige Kernfusionsanlagen wie ITER und DEMO werden aller Wahrscheinlichkeit nach in der H-mode (high confinement mode) betrieben. Durch das Auftreten einer Randtransportbarriere (ETB) weist dieser Betriebsmodus hohe Druck- und Stromgradienten am Plasmarand auf, welche freie Energie für magnetohydrodynamische Instabilitäten liefern. Eine Eigenschaft der H-mode ist das quasi periodische Auftreten von sogenannten ELMs (Edge Localized Modes) auf, die zur Zerstörung der ETB führen. Der Mechanismus, der die kritischen Größen die zur Instabilität eines ELMs führen momentan am besten beschreibt ist das Peeling-Ballooning Modell, in dem Plasmastrom getriebene Peeling Moden mit Druck getriebenen Ballooning Moden zu instabilen Peeling-Ballooning Moden koppeln.

Diese Masterarbeit beschäftigt sich mit der Untersuchung nichtlinearer Kopplung magnetischer Moden in ASDEX Upgrade Plasmaentladungen. In einem theoretischen Modell wird erst gezeigt, wie es zu Kopplungen von Moden in Wellen und demnach auch in Plasmafluktuationen kommen kann. In der Bikoheränzanalyse wird eine Methode diese Kopplungen zu diagnostizieren gezeigt. Ein Bikoheränz Algorithmus wurde entwickelt um beliebige zeitlich aufgelöste Signale zu analysieren. Mit der Anwendung von Fensterfunktionen und Dithering wurden zwei Methoden gefunden eine Verbesserung der Sensitivität bei Hintergrundrauschen und der Stabilität bei numerischen Fehlern zu erreichen.

Um die Funktion des Algorithmus bei der Analyse experimenteller Daten zu zeigen, wurden Signale von magnetischen Pick-up Spulen aus verschiedensten AUG Entladungen analysiert und dargestellt. Um nun die Kopplung verschiedener Moden vor, während und nach den ELMs zu untersuchen wurden die magnetischen Signale an die ELM Anfänge synchronisiert. Mit dieser Methode bleiben die ausschlaggebenden Eigenschaften der ELMs erhalten während sich unwichtige

Dinge wegmitteln. Die somit erhaltenen ELM-synchronisierten Daten wurden dann in eindeutige Phasen unterteilt und getrennt mit der Bicoherenzanalyse untersucht, wobei keine offensichtlichen Modenkopplungen in den einzelnen ELM Phasen gefunden wurden.

Contents

1. Introduction	1
1.1. Nuclear Fusion and the Tokamak Concept	3
1.2. ASDEX Upgrade and the H-Mode	6
1.3. Edge Localized Modes and MHD	8
2. Theoretical Background	11
2.1. Theoretical Description of Mode Coupling and Simulations	11
2.2. Signal Processing and Bicoherence	12
2.2.1. Continuous and Discrete Fourier Transformations	12
2.2.2. Implementation	18
2.2.3. Binning and Dithering	20
2.2.4. Windowing	22
2.2.5. Noise Stability	24
3. Experimental Analysis	27
3.1. Magnetic Measurements	27
3.2. Proof of Concept	28
3.3. Conditional Average: ELM-Synchronizing	31
3.4. Mode Number Determination	33
3.5. Bicoherence of the ELM Cycle	39
3.5.1. PRE - ELM Phase and Phase IV	42
3.5.2. ELM Phase	46
3.5.3. Phase I-III	48
4. Conclusions	51
4.1. Summary	51
4.2. Outlook	53

A. Danksagung	55
B. Bibliography	57

1. Introduction

The exploitation of artificial sources of energy is a key skill of human civilization. For the modern culture a life without energy, especially electric energy, is unthinkable. The availability of energy is accompanied by a scarceness of the required resources on one side and intrinsic risks on the other side. These menaces, in particular the shortness of natural resources and global warming, created by greenhouse gas (CO_2 , CH_4) emissions, will remain one of the largest challenges in the future. The plans to tackle these problems nowadays mostly include the expansion of renewable sources, like hydro- wind- or solar-energy and sometimes carbon capture.

A carbon neutral way to create electrical energy on a big scale are nuclear power plants. The attractiveness of nuclear energy arises from the strength of the nuclear force initiating nuclear reactions. The energy scale of such reactions is in the range of MeV/reaction. This is one million times higher than in the common chemical combustion reactions and therefore the same amount of fuel leads to a million times higher energy generation.

As shown in figure 1.1, nuclear reactions can theoretically produce a net energy gain, by splitting heavy nuclei like Uranium or Plutonium, or by fusing light nuclei to form heavier ones. Both these processes work up to mass numbers of around 50 – 60, where nuclei are most tightly bound.

Compared to nuclear fission, which is the standard nuclear energy source at the moment, fusion could theoretically produce a higher amount of energy per reaction. This can be seen in the binding energy difference, which indicates the maximum energy gain per reaction, is far greater, going from small atomic mass numbers $A = 2$ or $A = 3$ to medium sized nuclei $A = 50$, than the other way around.

Other advantages of using nuclear fusion for energy generation is that none of

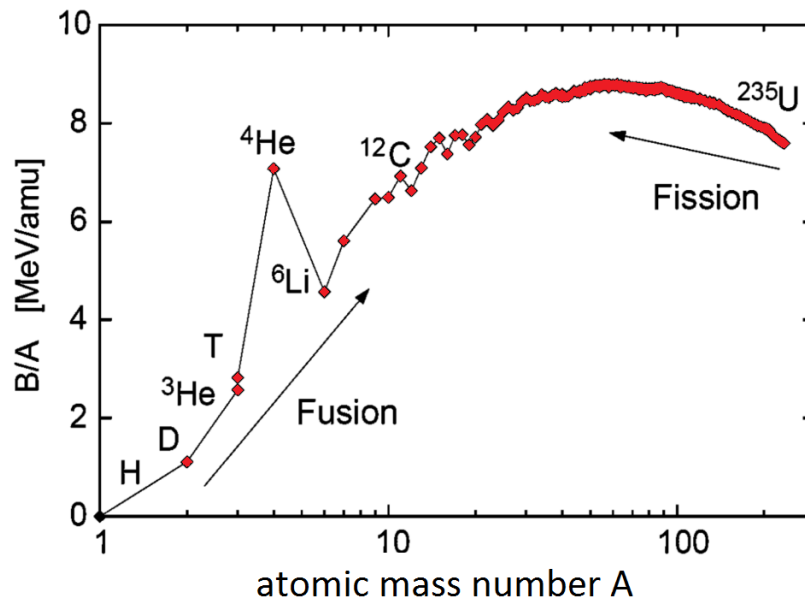


Figure 1.1.: Binding energy per nucleon over atomic mass A . According to the arrows, energy gain is possible by fusion of low A elements and fission of heavier elements. Slightly modified from [1]

the involved elements have half-life periods greater than a human lifetime and that there are no chain reactions that could get out of control.

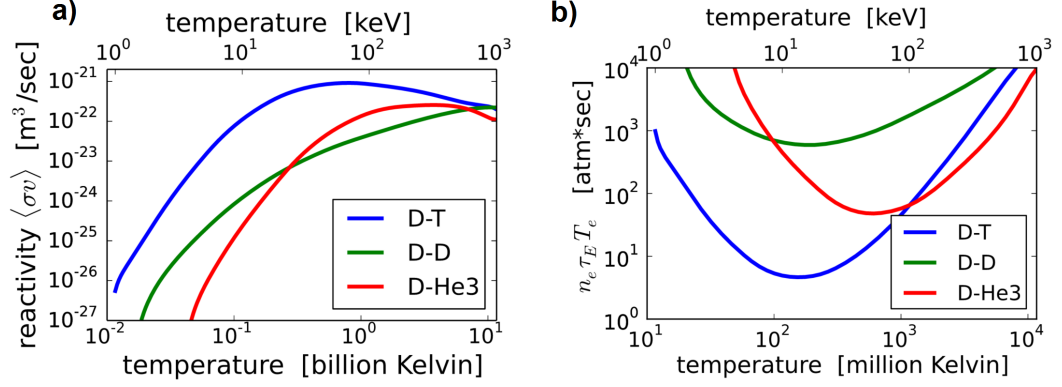


Figure 1.2.: Comparison of different fusion fuels in terms of a) the reactivity, where a higher number means a higher probability of a reaction occurring and b) the triple product $n\tau_E T$, where a plasma must exceed the plotted curves for fusion self-heating to overcome energy loss[3, 4]

1.1. Nuclear Fusion and the Tokamak Concept

Nuclear fusion has fascinated people since the 1920s [2]. Energy is released when nuclei of light elements (H, or its isotopes D and T) combine to form heavier elements (He). The fusion of four protons to one He nucleus, as it takes place in stars, involves the conversion of protons to neutrons via the weak force. A reaction's cross section, denoted σ , is the measure of the probability that a fusion reaction will happen. This depends on the relative velocity of the two nuclei. Higher relative velocities increase the probability. A good measure for the probability of a nuclear reaction occurring is the reactivity $\langle\sigma v\rangle$ which is an averaged product of the velocity dependent cross section σ and the particle velocity v . As can be seen in figure 1.2a), the reactivity, for the fusion of deuterium (D) with tritium (T) is, at this state, the most promising candidate for a fusion reactor with a cross section that is sufficiently high to be technologically feasible.



To realize fusion, the velocity and thus the temperature of the reacting particles has to be high enough to overcome the Coulomb barrier. For a future D-T fusion reactor most of the energy needed to keep the temperatures that high would

come from the kinetic energy of the created alpha particles (He^4). This process is called self-heating.

At temperatures over ten thousand Kelvin the electrons of hydrogen (and also D and T) atoms are no longer bound to the nuclei and hydrogen gas turns into a plasma. Lawson [5] gave a general measure for the conditions needed for a fusion reactor to become technologically feasible. He estimated that

$$nT\tau_E \geq 10^{21} \text{keVsm}^{-3} \quad (1.1)$$

where n represents the particle density, T temperature and τ_E the energy confinement time given by the total energy W divided by the power loss P_{loss} [6]. A representation of this so-called triple product is given in figure 1.2b) for different plasma fuels. If the plasma parameters exceed these self-heating conditions a net energy gain is possible.

One approach to achieve such high temperatures and densities, here on earth, is magnetic confinement. The central objective in magnetic confinement fusion is to constrain the D-T plasma by a magnetic field at sufficient temperature and density to reach a self-sustaining fusion plasma.

The highest developed approach in this field of research is the tokamak concept. It was originally designed in 1952 by Soviet physicists and is an acronym for the Russian translation of toroidal chamber in a magnetic field **tokamak**.

Because a tokamak, as seen on the left side of figure 1.4, consists of a toroidal vessel containing the plasma it is useful to describe occurring phenomena in toroidal coordinates, see figure 1.3.

Despite of their first letters, **theta** θ and **phi** φ , in analogy to cylindrical coordinates, θ represents the **p**oloidal and φ the **t**oroidal angle. Equations 1.2 show the transformation from Cartesian to toroidal coordinates and define the major radius R_0 , and the radial position inside the torus r .

$$\begin{aligned} x(\theta, \varphi) &= (R_0 + r \cos \theta) \cos \varphi \\ y(\theta, \varphi) &= (R_0 + r \cos \theta) \sin \varphi \\ z(\theta, \varphi) &= r \sin \theta \end{aligned} \quad (1.2)$$

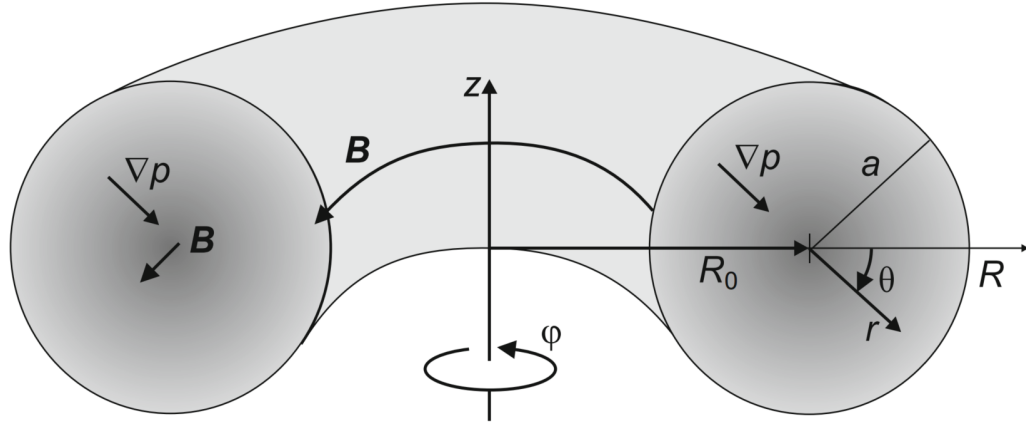


Figure 1.3.: Visualization of the toroidal coordinate system[1]

The defined chamber is surrounded by coils creating a toroidal (alongside the torus) magnetic field. In the center of the torus are additional field coils that act as a primary transformer circuit and induce a current in the plasma. This so-called plasma current creates a poloidal (perpendicular to the torus) magnetic field. Together these two fields result in a helical (screw shaped) magnetic field. To induce a plasma current that flows in one direction the current through the central solenoid has to change constantly. This necessity limits the duration of a plasma discharge and is therefore the reason a usual tokamak machine can only be operated in a pulsed manner.

In fusion experiments employing the tokamak configuration sufficient temperatures and densities (estimated with the lawson criterion) have already been reached. Although D-T seems to be the best fuel for a future fusion device, most experimental tokamaks run D-D campaigns. The reason for this is that Tritium is a radioactive material and therefore has obvious drawbacks for an experiment where diagnostics and other parts have to be changed very frequently. However, a large variety of plasma instabilities, which increase the transport of plasma across the magnetic field, have so far prohibited a net energy gain. Only the next generation experiments will be large enough to generate a surplus of energy. The world's largest fusion device ITER, is a tokamak and currently under construction in the south of France. The primary goal of ITER is to demonstrate the

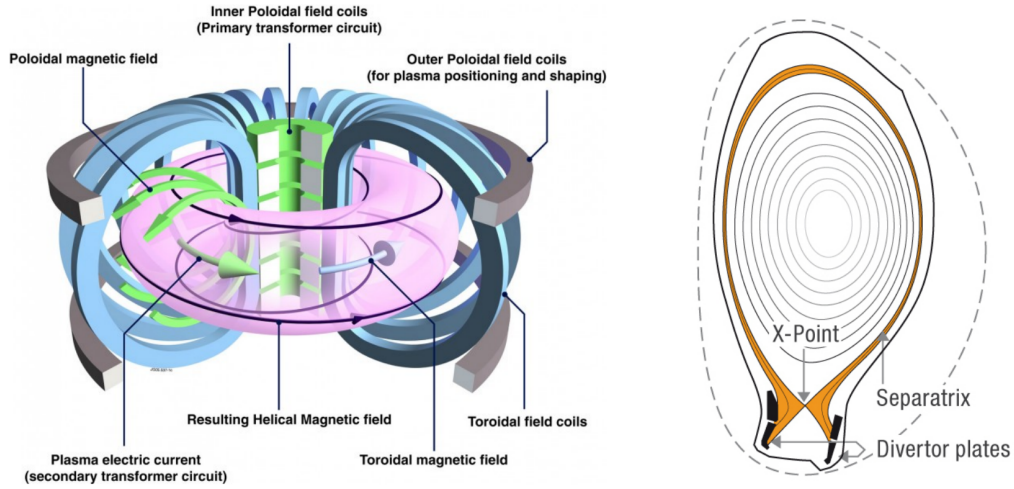


Figure 1.4.: Tokamak setup showing poloidal and toroidal field coils on the left and a poloidal cross section of a divertor experiment on the right. [7].

possibility of magnetic confinement fusion as a new energy source at large scales.

1.2. ASDEX Upgrade and the H-Mode

A key problem in fusion research is the power and particle load reaching the walls. The power load can mechanically damage the wall material and energetic ions from the plasma erode the surface by sputtering processes. To increase the distance between the hot central plasma and the zone of intense plasma-wall interaction, the so-called divertor configuration is employed. In these designs, as seen on the right side of figure 1.4, magnets pull the lower edge of the plasma to create a small region where the outer edge of the plasma hits specially designed target plates. To achieve that the magnetic field is configured to create an X-point at the last closed flux surface which is often called separatrix. The zone outside of the separatrix is called scrape-off layer (SOL). Modern reactors try to create plasmas with D-shaped cross-sections (“elongation” and “triangularity”) so the lower edge of the D is a natural location for the divertor. The divertor allowed higher heating powers compared to limiter setups. On ASDEX (axial symmetrical divertor experiment), which was one of the first tokamaks with a divertor setup, *Wagner et al.* [8] observed a spontaneous transition from a low confine-

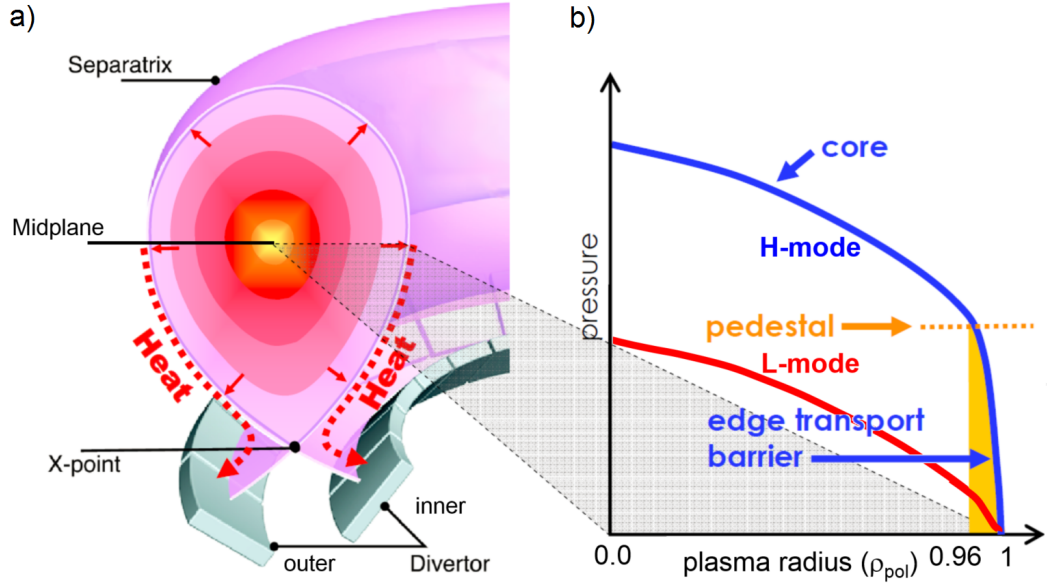


Figure 1.5.: a) Poloidal cross section of a tokamak with divertor setup, b) plasma pressure profile for L and H-mode over the normalized plasma radius ρ_{pol} with formation of the edge transport barrier and the pedestal.[10]

ment (L-mode) to a high confinement (H-mode) state where τ_E was enhanced by a factor of 2 or more. This happened when the heating power was above a certain threshold. On ASDEX's successor experiment, ASDEX Upgrade (AUG), it was demonstrated [9] that this transition occurs due to the formation of a sheared flow layer and an associated edge radial electric field. These phenomena lead to the formation of an **edge transport barrier** (ETB) which causes an increase in pressure for the whole plasma and steeper density and temperature gradients at the plasma edge (see figure 1.5). The core pressure gradients of H-mode plasmas do not significantly change in comparison to L-mode plasmas, but the steep edge gradients lead to an elevation of the overall pressure. This global increase of pressure profiles is called pedestal.

Historically, the discovery of the H-mode and its improved confinement time was a very big leap to the realization of a feasible nuclear fusion reactor. H-mode will most certainly be the operational mode for ITER.

1.3. Edge Localized Modes and MHD

The steep gradients associated with ETBs, mentioned in the previous chapter, provide a source of free energy for **magnetohydrodynamic** (MHD) instabilities. The discovery of the H-mode regime also brought up a new type thereof.

Edge localized modes (ELMs) are periodically occurring instabilities that expel particles and energy from the plasma edge into the SOL in short time intervals of around 1ms [11]. They cause high heat loads at the divertor and the first wall but also flush out impurities from the plasma core, which improves the confinement.

A theoretical approach to understand these instabilities is provided by MHD stability analysis. In such calculations a simplified form of the MHD equations (Maxwell's equations + fluid mechanics) is solved using periodic functions with given mode numbers.

Starting from a magnetic field configuration with all parameters in equilibrium these analyses take a small perturbation of the plasma ξ and put it to a stability test. It checks if the plasma only oscillates and relaxes back to equilibrium, or if the perturbation grows with a given growth rate γ .

A nice analogy for a stability analysis is a marble on a rippled board. The marble can be in equilibrium sitting on a hill or in a valley. The difference between those two states is, that the 'marble on the hill' state is highly unstable, meaning a small perturbation will lead to oscillations around a different state while small perturbations of the 'marble in the valley' state will converge back to the original state.

To describe plasma parameters and their perturbations Fourier decomposition leads to the definition of the **toroidal mode number** n and the **poloidal mode number** m .

The difference between linear and non-linear stability analyses lies in the used perturbation. If the perturbation is a simple periodic function with only one n , frequency ω and growth rate γ (here called linear growth rate), e.g.

$$\xi(t) = \xi_0 + \xi_1 e^{(i\omega + \gamma)t + 2\pi i \varphi n} \quad (1.3)$$

we speak of a linear analysis. If more than one mode number is considered

$$\xi(t) = \xi_0 + \xi_1 e^{(i\omega_1 + \gamma_1)t + 2\pi i \varphi n_1} + \xi_2 e^{(i\omega_2 + \gamma_2)t + 2\pi i \varphi n_2}, \quad (1.4)$$

is still a linear function, but higher orders of ξ will lead to mixed terms containing $n_1 + n_2$, i.e. mode coupling.

It was found, in linear stability analysis, that a combination of pressure and current driven instabilities, called peeling-ballooning (PB) instabilities, could lead to ELM like periodic instabilities.

In the H-Mode the pressure gradient steepens at first and clamps at a certain point, however, the pedestal width still widens and therefore the pedestal height still builds up [12]. At a specific pressure value the plasma becomes unstable due to ballooning modes. Meanwhile, this pressure gradient drives an additionally occurring bootstrap current, which at a certain threshold leads to unstable peeling modes.

The PB-Model can not fully describe the dynamics of an ELM nor its spatial structure, because non-linear effects play a significant role. As an example figure 1.6a) shows the filamentary structure of an ELM measured by a high speed camera at MAST while figure 1.6b) shows a simulated picture created using a non-linear ballooning code. The simulation reproduces the filamentary structure observed by the cameras with astonishing precision.

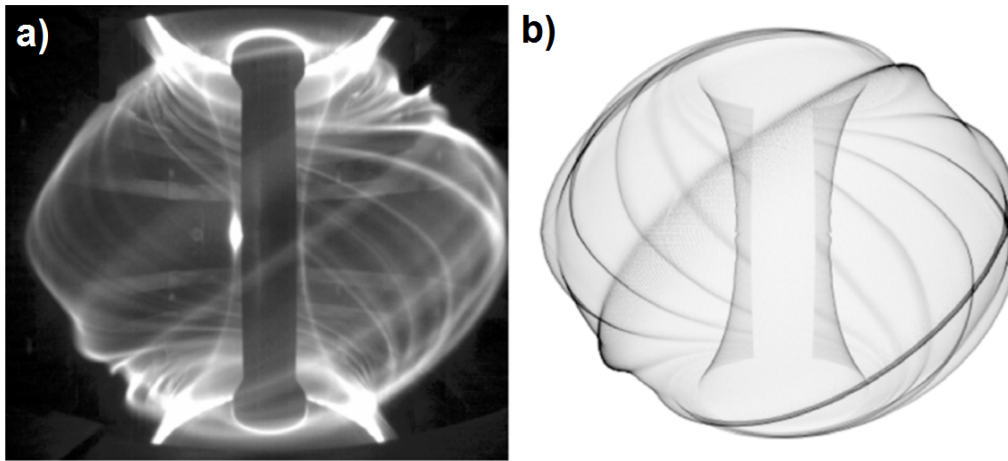


Figure 1.6.: (a) High-speed video image of the MAST plasma obtained at the start of an ELM.
 (b) The predicted structure of an ELM in the MAST tokamak plasma geometry, based on the non-linear ballooning mode theory.[7]

2. Theoretical Background

As mentioned in chapter 1.3 the fusion plasma and its perturbations can be described by a superposition of modes. Theoretically these modes can interact with each other, which is called mode coupling. It is suspected, that this non-linear process happens in the inter ELM cycle [13]. This chapter gives a simple model of non-linear coupling of plasma modes and, with bicoherence, a method to visually represent these couplings.

2.1. Theoretical Description of Mode Coupling and Simulations

Krebs et al. [14] demonstrated a simple quadratic model to describe the coupling of different modes in AUG.

JOREK is a simulation code that solves the resistive MHD equations and shows the time evolution of energy content for selected mode numbers. With these $E_n(t)$ values it is possible to calculate corresponding growth rates

$$\gamma_n = \frac{1}{2} \frac{d \log E_n}{dt}, \quad (2.1)$$

which lead to information about the stability of the modes.

Following [14], an interaction picture, that allows transfer of energy between different modes, is constructed. Consider a wave consisting of two contributions with different mode numbers n_1 and n_2 and amplitudes A_1 and A_2 , respectively,

$$A(\omega) = A_1 \cos(n_1 \omega) + A_2 \cos(n_2 \omega) \quad (2.2)$$

Non-linear Terms in $A(\omega)$ lead to a mixture of the two modes, where the simplest

term is quadratic and yields

$$\begin{aligned}
A^2(\omega) &= [A_1 \cos(n_1\omega) + A_2 \cos(n_2\omega)]^2 \\
&= A_1^2 \cos^2(n_1\omega) + A_2^2 \cos^2(n_2\omega) + \\
&\quad + A_1 A_2 \cos[(n_1 - n_2)\omega] + A_1 A_2 \cos[(n_1 + n_2)\omega]
\end{aligned} \tag{2.3}$$

Hence, two modes with mode numbers $(n_1 - n_2)$ and $(n_1 + n_2)$ are generated. According to this, energy transfer can take place between three modes, if $n_3 = n_1 + n_2$ or if $n_3 = n_1 - n_2$. This so-called **three wave coupling** and its illustration is the main topic of this thesis.

2.2. Signal Processing and Bicoherence

The information contained in a digitally acquired signal at discrete time points $x_n(t_n) = x[t]$ is far greater than is recognizable at a first glance. Additional information can be extracted using different signal processing (SP) techniques. The ideal SP tool to visualize coherent non-linear coupling of frequency components is the Bicoherence method which will be derived in this chapter.

Bicoherence and bispectra are higher order spectra (HOS) which were first introduced by Tukey [15] in the early 1960s to analyze wave coupling phenomena. The method is not uncommon in plasmaphysics, see [16, 17, 18], but is apart from a few exceptions [19, 20], not used on AUG data. Therefore a big focus was to really understand the basics of the method and to test them thoroughly.

2.2.1. Continuous and Discrete Fourier Transformations

Higher order spectra are defined in terms of Fourier coefficients, therefore it is important to recall some basic definitions.

The Continuous Fourier Transform (CFT) $X(f)$ of a time resolved signal $x(t)$ is defined as

$$X(f) = \int_{-\infty}^{\infty} x(t) e^{i2\pi ft} dt. \tag{2.4}$$

It transforms the signal from the time into the frequency domain and therefore contains information about the Fourier modes contained in the signal.

It's numerical counterpart, the discrete Fourier transform (DFT), is defined as

$$X[k] = \sum_{j=0}^{N-1} x[j] e^{-2\pi i \frac{jk}{N}} \quad (2.5)$$

where the real discrete time series, $x[j]$, is parameterized by index j where $j = 0, \dots, N-1$, the frequency domain signal $X[k]$, is parameterized by index k where $k = 0, \dots, N-1$ and the total number of points in the signal is N . The sampling frequency as well as the total signal duration impose limits on the frequency content of a discrete signal. The highest resolvable frequency, referred to as the Nyquist frequency, f_N , is, under ideal conditions, given by half of the sampling frequency f_s , i.e.

$$f_N = \frac{f_s}{2} \quad (2.6)$$

and the frequency resolution Δf is determined by the number of points in the signal N , and the time resolution Δt as

$$\Delta f = \frac{2}{N\Delta t} \quad (2.7)$$

Figure 2.1 shows an example of the discrete Fourier transformation of a signal $x[j] = \sin(2\pi n_1 j) + \sin(2\pi n_2 j)$ with $n_1 = 0.1$ and $n_2 = 0.3$ with $N = 100$ points. The absolute value of the Fourier coefficients $|X[k]|$ shows peaks at $k = 10, 30, 70$ and 90 which correspond to $n_1 N, n_2 N, (1 - n_1)N$ and $(1 - n_2)N$.

A corresponding physical example is given in figure 2.2 where $x[t] = \sin(2\pi f_A t) + \sin(2\pi f_B t)$ with $f_A = 10\text{Hz}$ and $f_B = 30\text{Hz}$ and t goes from $t = 0\text{s}$ to $t = T = 1\text{s}$ in $\Delta t = 0.01\text{s}$ steps. This is equal to a sampling frequency of $f_s = 100\text{Hz}$. The difference between figure 2.1 and figure 2.2 lies in the representation of the Fourier transformed signal. While in the first example $|X[k]|$ is simply computed using equation 2.5, the DFT performed in the second example also shifts the components, to get the real physical interpretation. The k values from 0 to $N/2$ represent the corresponding frequencies from 0 to f_N but the values of k ranging from $N/2 + 1$ to N actually represent the frequencies from $-f_N$ to 0 and not, as

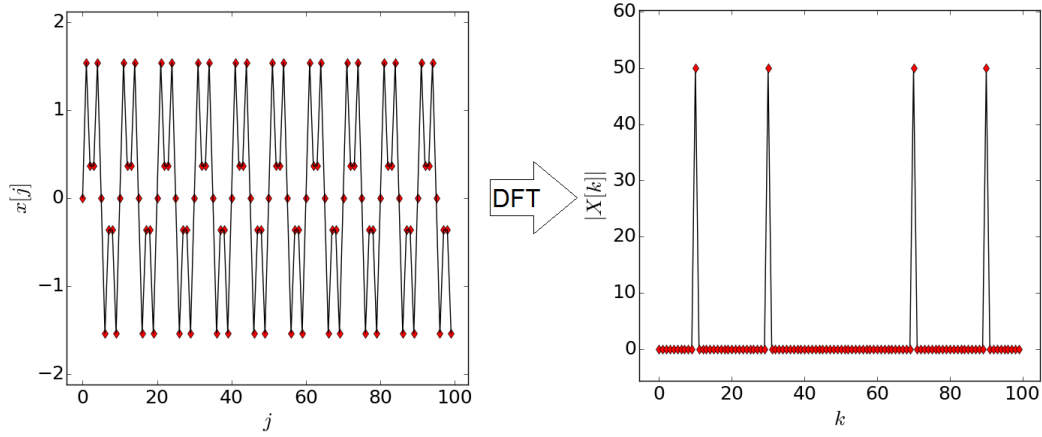


Figure 2.1.: Numerical example of a discrete Fourier transformation of $x[j] = \sin(2\pi j \cdot 0.1) + \sin(2\pi j \cdot 0.3)$

one could expect, the frequencies from f_N to $2f_N$.

It is important to note, that for real values of $x[j]$, $X[k]$ will be symmetrical, meaning

$$\begin{aligned} X[N - k] &= X[k]^* \\ X[-f] &= X[f]^*, \end{aligned} \quad (2.8)$$

where the X^* operation stands for complex conjugation.

In the generalized sense of signal processing, the energy of a signal $x(t)$ is given by

$$E(t) \propto \int_{-\infty}^{\infty} |x(t)|^2 dt. \quad (2.9)$$

Considering equation 2.4 one can easily see, that equation 2.9 can also be written as

$$E(t) \propto \int_{-\infty}^{\infty} |X(f)|^2 df \quad (2.10)$$

and therefore

$$S_{XX}(\omega) = |X(f)|^2 \quad (2.11)$$

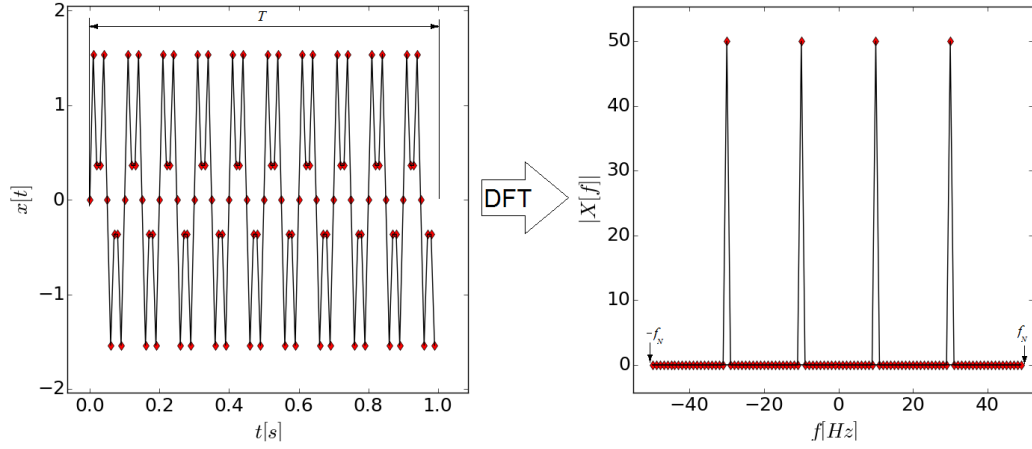


Figure 2.2.: Discrete Fourier transformation of a time resolved signal $x[t] = \sin(2\pi f_A t) + \sin(2\pi f_B t)$ with $f_A = 10\text{Hz}$ and $f_B = 30\text{Hz}$

can be defined as power spectral density.

In the time domain one can define the auto-correlation function $r_{xx}(t)$, also known as the second order cumulant, as

$$r_{xx}(t) = \int_{-\infty}^{\infty} x(t + \tau)^* x(\tau) d\tau = \int_{-\infty}^{\infty} x(t - \tau) x(\tau)^* d\tau \quad (2.12)$$

where $x(t)^*$ represents the complex conjugate of $x(t)$. $S_{XX}(\omega)$ and $r_{xx}(t)$ are connected via the Wiener Khinchin theorem

$$S_{XX}(f) = \int_{-\infty}^{\infty} r_{xx}(t) e^{i\omega t} dt \quad (2.13)$$

showing that the power spectral density is the Fourier transformed auto-correlation function.

Increasing the order of the cumulant one arrives at the third order momentum

$$r_{xxx}(t) = \int_{-\infty}^{\infty} \int_{-\infty}^{\infty} x(t + \tau_1)^* x(t + \tau_2)^* x(\tau) d\tau_1 d\tau_2 \quad (2.14)$$

with its Fourier transform being the bispectrum

$$B(f_1, f_2) = X(f_1)X(f_2)X(f_1 + f_2)^* \quad (2.15)$$

which is only > 0 if the spectrum contains amplitudes at the frequencies f_1 , f_2 and $f = f_1 + f_2$. The **three – wave – coupling** is fulfilled in the simplest non-linear coupling mechanism, quadratic coupling. As can be seen in equations 2.2 and 2.3 a simple quadratic ansatz already shows the three-wave-coupling condition fulfilled.

To project the bispectrum to an interval $0 < f(B(f_1, f_2)) < 1$ and to add phase correlation information and more statistics one defines the auto-bicoherence

$$BIC(f_1, f_2) = \frac{\langle |B(f_1, f_2)| \rangle^2}{\langle |X(f_1 + f_2)|^2 \rangle \langle |X(f_1)X(f_2)|^2 \rangle} \quad (2.16)$$

The auto-bicoherence as defined in equation 2.16 has a lot of symmetries as seen in figure 2.3. It is symmetric around the line given by $f_1 = f_2$ because

$$B(f_1, f_2) = B(f_2, f_1) \quad \text{and} \quad BIC(f_1, f_2) = BIC(f_2, f_1)$$

and symmetric around the line given by $f_2 = -f_1$ because of equation 2.8. These symmetries as well as some examples are explained below.

Figure 2.3 shows the full bispectrum of a signal $x(t) = \sin(2\pi f_A t) + \sin(2\pi f_B t)$ containing the frequencies $f_A = 10\text{Hz}$ and $f_B = 20\text{Hz}$. It should again be emphasized, that because $x(t) \in \mathbb{R}$, the spectrum $X(f) = FFT(x(t))$ is symmetric around $f = 0$ meaning the Fourier components have the same amplitude for $f = x$ and for $f = -x$, and that for a peak to show up in the auto-bispectrum $B(f_1, f_2)$, the Fourier transformed signal has to have non-zero amplitude at the frequencies f_1, f_2 and $f_1 + f_2$. The three-wave-coupling condition is therefore realized 6 times:

f_1	f_2	$f_1 + f_2$
-20Hz	10Hz	-10Hz
-10Hz	-10Hz	-20Hz
-10Hz	20Hz	10Hz
10Hz	-20Hz	-10Hz
10Hz	10Hz	20Hz
20Hz	-10Hz	10Hz

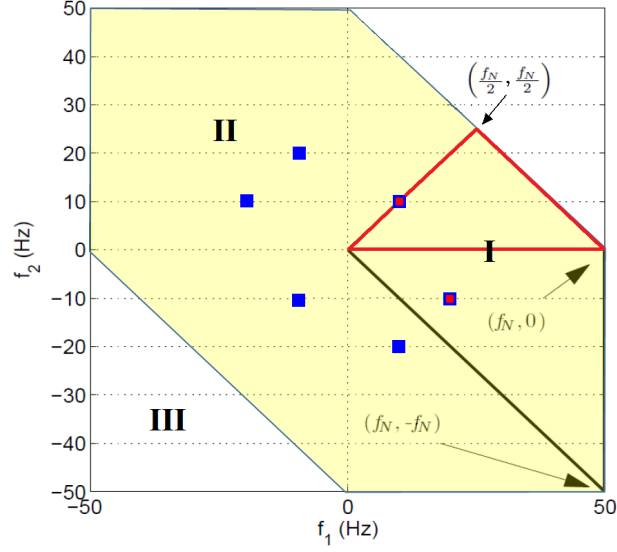


Figure 2.3.: Bicoherence of signal containing frequencies 10Hz and 20Hz. Domain of the auto-bispectrum (yellow area marked with *II*), can be reduced to the contained domain (marked with *I*). Area *III* represents the not computable area where $|f_1 + f_2| > f_N$.

All 6 frequency triples are equivalent and could be represented by one point ($|f_1| = 10\text{Hz}$, $|f_2| = 10\text{Hz}$, $|f| = 20\text{Hz}$) lying on the edge of the triangle limited by the f_1 axis and the point $f_1 = f_2 = \frac{f_N}{2}$, which is marked by the red lines in figure 2.3. However for better visibility the domain of the auto-bicoherence is in this thesis chosen to be the skewed right angled trapezoid given by the points $(f_1, f_2) = (0\text{Hz}, 0\text{Hz})$, $(\frac{f_N}{2}, \frac{f_N}{2})$, $(f_N, 0\text{Hz})$ and $(f_N, -f_N)$ shown as sector *I* of figure 2.3. The points in area *II* of figure 2.3 can all be interpreted as permutations of the 3-frequency points in area *I*. Therefore it is sufficient to compute the bispectrum of area *I*.

Simple mirroring at the line $f_1 = f_2$ and then at the line $f_1 = -f_2$ leads to the completion and therefore the full bicoherence. In area *III* the sum of the frequencies $f_1 + f_2$ is greater than the Nyquist frequency f_N and can not be computed. This leads to the full domain of the auto-bispectrum having a hexagonal shape.

2.2.2. Implementation

In the work for this thesis, a python code was created, that contains functions to calculate and plot the auto-bicoherence of a given time resolved signal. The sequence of processes needed to calculate the bicoherence will be discussed in this chapter. At first the signal is split up into bins for statistical purposes. The code also has the ability to apply a windowing function to the measured data to prevent spectral leakage (chapter 2.2.4) . After subtracting the bin-mean value of every bin all of them are being Fourier transformed and cut at the desired maximum frequency. This process is followed by calculating the triple product as given in equation 2.15 for every possible combination of f_1 and f_2 . For long time series or a high number of bins, these calculations take a lot of time and memory. Therefore the code exploits the symmetries of the bicoherence, as discussed in the previous chapter, and calculates the triple products only on the confined domain I , as shown in figure 2.3. When all these complex products are calculated the triple products are normalized (equation 2.16), resulting in the bicoherence.

In summary the auto-bicoherence calculation works as follows:

- Start with a signal $x[t]$, where $t = [0, \Delta t, \dots, T - \Delta t, T]$
- 1. Split signal into i bins with length N : x_i
- 2. Subtract the mean: $x_i[t] - \overline{x_i[t]}$
- 3. Apply window: $\left(x_i[t] - \overline{x_i[t]}\right) w[t]$
- 4. Perform FFT: $X_i = \mathbf{FFT} \left[\left(x_i[t] - \overline{x_i[t]}\right) w[t] \right]$
- 5. Compute Bispectrum: $B_i[f_1, f_2] = X_i[f_1]X[f_2]X[f_1 + f_2]^*$ in the domain
 - Repeat steps 1-5 for every bin
 - Normalize $B([f_1, f_2])$ to get $BIC[f_1, f_2]$

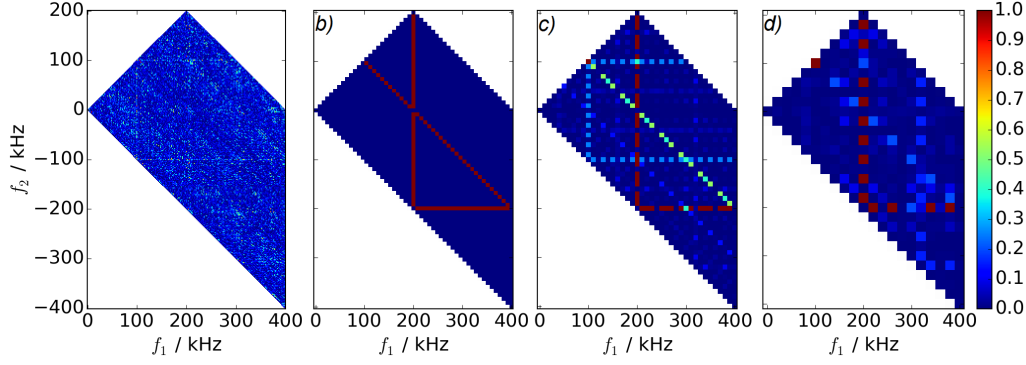


Figure 2.4.: Auto-bicoherence $BIC(f_1, f_2)$ of $x[t] = \sin(2\pi f_A t) + \sin(2\pi f_B t)$ with varying bin sizes a) 20 bins á 1000 points, b) 80 bins á 500 points, c) 100 bins á 400 points, d) 100 bins á 200 points

2.2.3. Binning and Dithering

A toy-model was created to test the built bicoherence algorithm. This allowed to simulate signals with different frequency and phase components and test the different parameters of a bicoherence analysis in detail. As a first example a simple test function $x[t] = \sin(2\pi f_A t) + \sin(2\pi f_B t)$ with $f_A = 100\text{kHz}$ and $f_B = 200\text{kHz}$ was created. Figure 2.4 shows the auto-bicoherence $BIC(f_1, f_2)$ where n stands for the number of bins into which the time series is split up. For the displayed case t was chosen to be a discrete array from $[0.5\mu\text{s}, 1\text{s}, \dots, 1\text{ms}]$ containing 20000 time-points separated by time steps of $\Delta t = 0.5\mu\text{s}$, which leads to $f_N = \frac{1}{2\Delta t} = 1\text{MHz}$ and a maximum frequency resolution of $\Delta f = \frac{1}{N\Delta t} = 1\text{kHz}$. As can be seen in chapter 3 these values were chosen to match the time and frequency resolutions of the magnetic pickup coils of AUG.

None of the calculated bicoherences show the desired output of a single point highlighted at the frequency points $(f_1, f_2) = (f_A, f_A) = (100\text{kHz}, 100\text{kHz})$ and $(f_1, f_2) = (f_B, -f_A) = (200\text{kHz}, -100\text{kHz})$ that satisfy the three-wave-coupling condition and are located in the reduced domain. The information that can already be seen in figure 2.4 is, that clearly the frequency resolution Δf is reduced when decreasing the number of points per bin, by increasing the number of bins. Also the noise in the bicoherence reduces, when taking more bins and therefore more statistics.

To reduce the so-called quantization error that's caused by the appearance

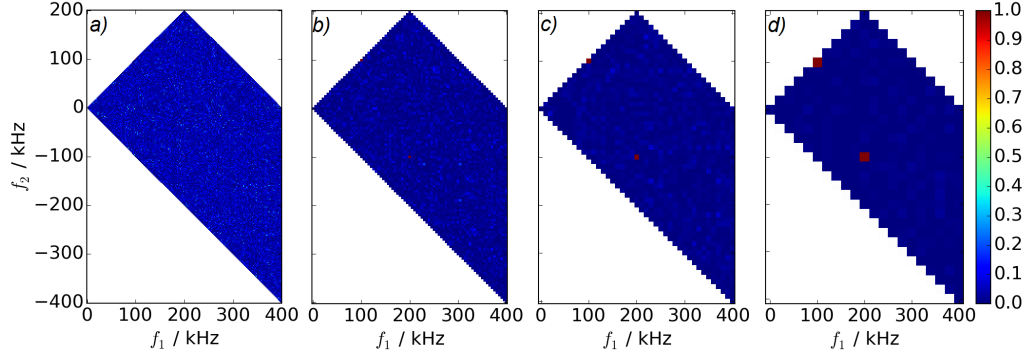


Figure 2.5.: Auto-bicoherence $BIC(f_1, f_2)$ of $x[t] = \sin(2\pi f_A t) + \sin(2\pi f_B t) + 0.1n[t]$ and for different bin sizes a) 20 bins á 1000 points, b) 80 bins á 500 points, c) 100 bins á 400 points, d) 100 bins á 200 points

of abrupt discontinuities in the signal due to the binning and can be seen in figure 2.4 as numerical artifacts, a small random noise signal was added to the original signal. The technique used to reduce this problem is called **dithering** or **pseudo random noise quantization** and is often used in signal processing for audio and video signals, see [21].

The signal was therefore modified to $x[t] = \sin(2\pi f_A t) + \sin(2\pi f_B t) + A \cdot n[t]$, where $n[t]$ is an array of random numbers limited by 0 and 1. Varying noise amplitudes A have big effects on the bicoherence of test signals (see chapter 2.2.5) The bicoherences plotted in figure 2.5 show the expected results. As already suspected from figure 2.4, the frequency resolution as well as the noise decreases when the number of bins is increased.

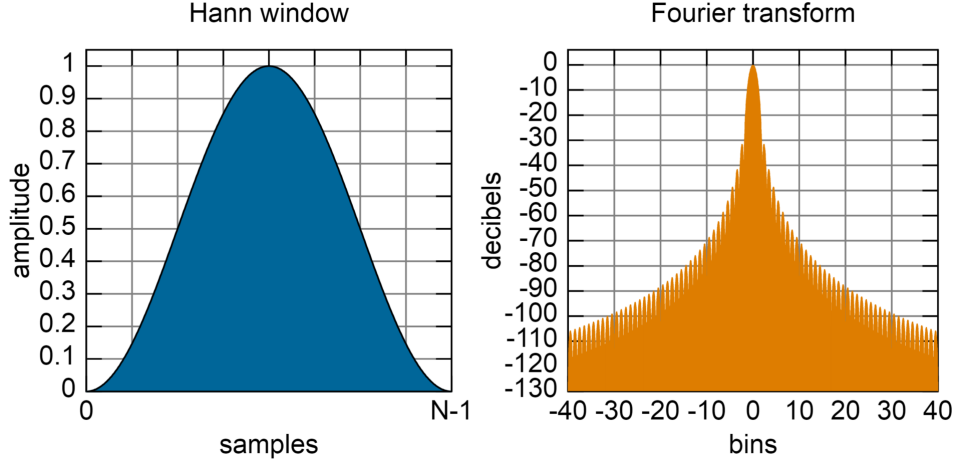


Figure 2.6.: Temporal and Fourier properties of the Hann window[22]

2.2.4. Windowing

Another widely used technique in signal processing is windowing $x_w[t] = x[t]w[t]$, where a windowing function is multiplied with the signal increase periodicity. It dampens often occurring discontinuities at the boundaries of time resolved signals and reduces the spectral leakage effect. The windowing function used in this thesis was the Hann window $w(n) = (1 - \cos(\frac{2\pi n}{N-1}))$. Its time and frequency properties are displayed in figure 2.6. Since the equivalent of multiplication in the time domain is, convolution in the frequency domain, the analyzed spectrum appears to be convoluted with the window spectrum. This can lead to unwanted effects, if the very low window frequency couples to frequencies contained in the signal.

It was found that windows broaden the frequency peaks in the Fourier spectrum, compare peaks in figure 2.5a) - d) to figure 2.7 and thus also lead to better detectability of points in the bicoherence. Figure 2.7 shows the mentioned coupling of the signal frequencies (100kHz and 200kHz) to the maximum window frequency ($f_w \approx \frac{1}{2 \cdot \text{binsize} \cdot \Delta t}$ Hz). These additional points in the bicoherence do not represent real couplings, because the window frequency of the Hann window f_w is approximately $\frac{1}{4}$ of the frequency resolution Δf and should therefore not be visible in the signal. The additional points can be disposed of by running the algorithm fist without the window applied and then running it for a second

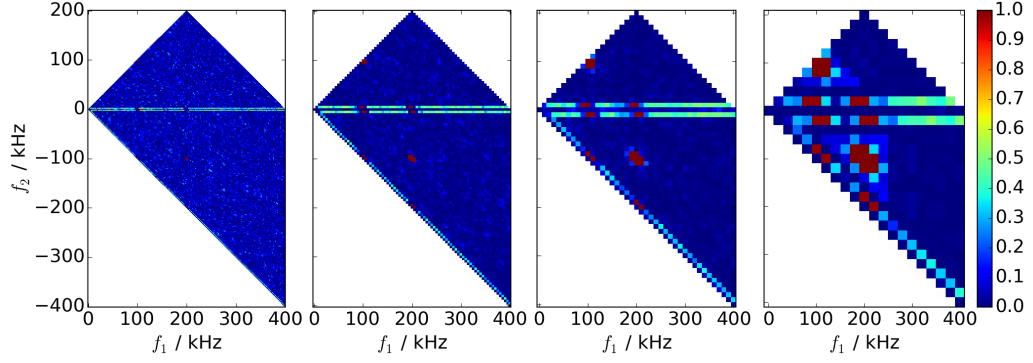


Figure 2.7.: Auto-bicoherence $BIC(f_1, f_2)$ of $x[t]w[t]$ where $x[t] = \sin(2\pi f_A t) + \sin(2\pi f_B t) + 0.1n[t]$ and $w[t]$ a Hann window, for different bin sizes a) 20 bins á 1000 points, b) 80 bins á 500 points, c) 100 bins á 400 points, d) 100 bins á 200 points

time with the applied window. The reason for this problem and why the solution works is not totally clear. One idea is that the additional points in the bicoherence appear due to the divisions in the normalizing process, where very small quantities are divided by even smaller quantities. This can lead to numerical problems which are probably solved by running the algorithm first without windowing. The auto-bicoherence values with applied window in the second run are shown in figure 2.8. The windowed auto-bicoherence looks very similar to the auto-bicoherence without windowing (figure 2.5) but, as mentioned, the peaks appear to be broader and therefore more visible. The noise sensitive nature of this so-called peak broadening will be discussed in the next chapter.

The Hann window provided in the demonstrated algorithm, figure introduce additional low frequencies to the spectrum and can create artificial three-wave-couplings in the bicoherence that can be seen in 2.7c) . For this reason, and for the very noise sensitive nature (see chapter 2.2.5) of windowed signals, this technique has to be used with great caution.

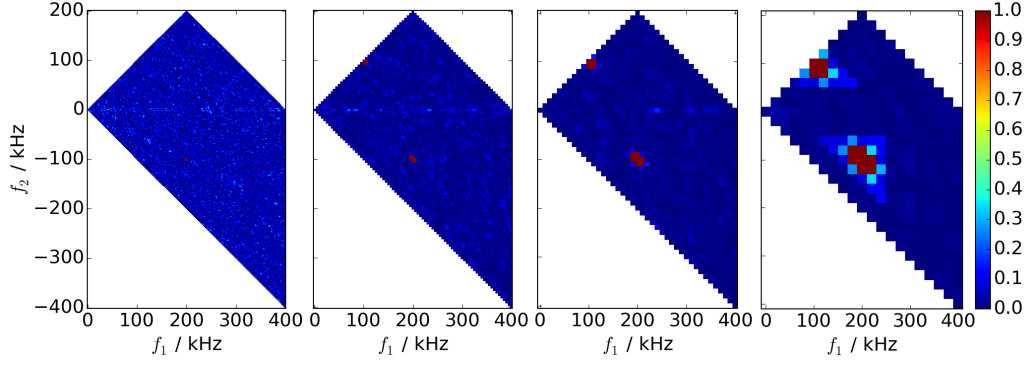


Figure 2.8.: Auto-bicoherence $BIC(f_1, f_2)$ of $x[t] = \sin(2\pi f_A t) + \sin(2\pi f_B t) + 0.1n[t]$ for different bin sizes a) 20 bins á 1000 points, b) 80 bins á 500 points, c) 100 bins á 400 points, d) 100 bins á 200 points

2.2.5. Noise Stability

To test the noise stability of the algorithm, the intensity A of the added random noise was varied.

$$x_i[t] = \sin[2\pi f_A t] + \sin[2\pi f_B t] + A \cdot n[t]$$

Figure 2.9 shows that the bicoherence is stable and shows the expected results, $BIC(f_1, f_2) = BIC(f_A, f_A) \cong 1$ where the three-wave-coupling condition $f_2 = f_1 + f_1$ is fulfilled, up to a noise amplitude 5 times as high as the signal amplitude. This is due to the fact, that the random noise has no fixed phase relation. It was also tested, that adding a constant random phase to every bin of the ensemble leads to $BIC(f_1, f_2) = 0$ for all frequencies f_1 and f_2 , whereas this operation does not change the power spectrum at all. This also suggests, only bins with a fixed phase relation will contribute to the bicoherence.

As mentioned in chapter 2.2.4, using a windowing function can lead to peak broadening. This effect can be seen in figure 2.10 where the peak broadening decreases with increasing noise amplitude. This is probably due to a combination of the already mentioned binning discontinuities and the leakage effect.

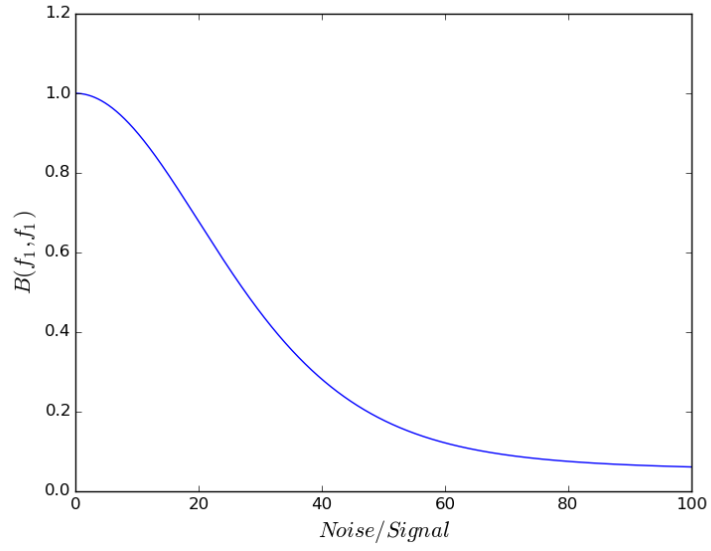


Figure 2.9.: $B(f_1, f_1)$ where $f_2 = f_1 + f_1$ for varying noise intensity

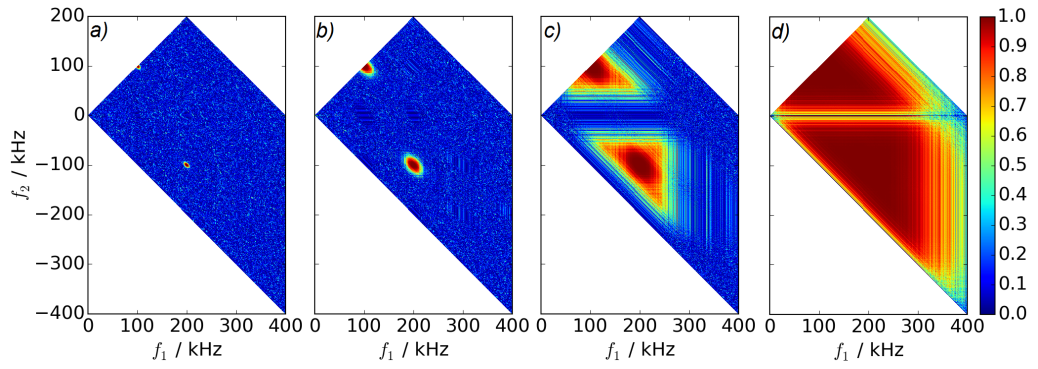


Figure 2.10.: Noise stability of the windowed signal with noise intensities a) $A = 10^{-3}$, b) $A = 10^{-4}$, c) $A = 10^{-5}$, d) $A = 10^{-6}$

3. Experimental Analysis

To detect non-linear coupling of different plasma modes experimental data from ASDEX Upgrade were analyzed with the bicoherence algorithm. This chapter shows how magnetic data is obtained and analyzed.

3.1. Magnetic Measurements

To measure the magnetic field B or its fluctuations $\frac{dB}{dt}$, so-called Ballooning Coils are installed in ASDEX Upgrade. The varying magnetic flux densities induces a measurable voltage signal in the coils, according to Faraday's law of induction

$$U = \frac{d\Phi}{dt} \quad \text{with} \quad \Phi = \int \vec{B} d\tilde{A}. \quad (3.1)$$

The magnetic diagnostics at ASDEX Upgrade consists of many such coils arranged in different poloidal and toroidal positions in the tokamak, measuring the poloidal or the radial magnetic field. Magnetic instabilities appear as fluctuations in the radial magnetic field B_r . They can be observed with the radial magnetic field coils B31-xx (often called ballooning coils), which are placed at the outboard midplane. Figure 3.1 shows that they are very close to the plasma, where 3.1a) shows the coil positions in a toroidal cross section of AUG and 3.1b) a poloidal one. The signals of the B31-xx coils are sampled at a 2MHz rate and are then digitized with 14bit analog digital converters that contain a low pass at 512kHz [23]. Thus the Nyquist frequency of the signals is 1MHz but frequencies over 512kHz are affected by the low pass.

To obtain the magnetic field B_r from the measured voltage $U \propto \frac{dB}{dt}$, the signal was integrated using a simple trapezoidal integration algorithm.

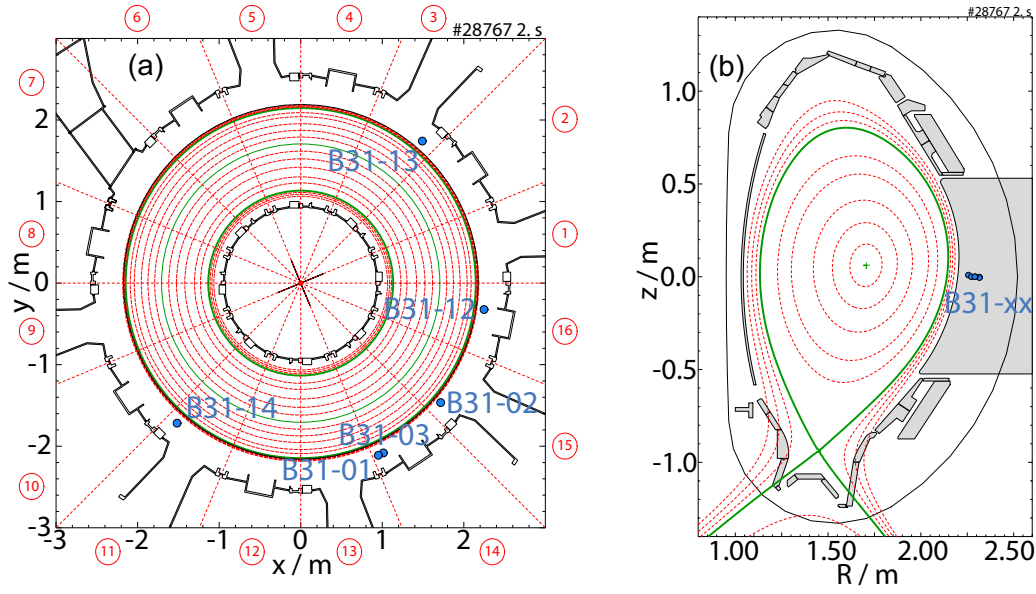


Figure 3.1.: Position of the toroidally distributed ballooning pick-up coils at the outer mid-plane (a) in the toroidal and (b) mapped to a poloidal cross section of ASDEX Upgrade[24]

3.2. Proof of Concept

To test the auto-bicoherence algorithm on experimental data, AUG discharge #28061 was analyzed. The ballooning coil B31-14 signal of this discharge contains a highly developed mode at around 16kHz and its first harmonic at 32kHz. The bicoherence of such signals should have a clearly visible point at $(f_1, f_2) = (16\text{kHz}, 16\text{kHz})$ and one at $(f_1, f_2) = (32\text{kHz}, -16\text{kHz})$. As one can see in figure 3.2, which shows the picked up signal in a) and the power-spectrogram in b), the mode is not exactly at 16kHz but varies from about 14kHz to 18kHz and multiples thereof. These broader frequency peaks lead to lines instead of points in the bicoherence, because the three-wave-coupling condition is met for a range of frequencies rather than sharp frequency points.

In figures 3.3 and 3.4 one can see the auto-bicoherence of the magnetic signal from coil B31-14 with the expected lines. To show that the concepts discussed in chapter 2.2 still apply for experimental data, the bicoherence was calculated for varying bin number, added random noise and with or without Hann window used. Figure 3.3 shows the auto-bicoherence of the measured signal split into

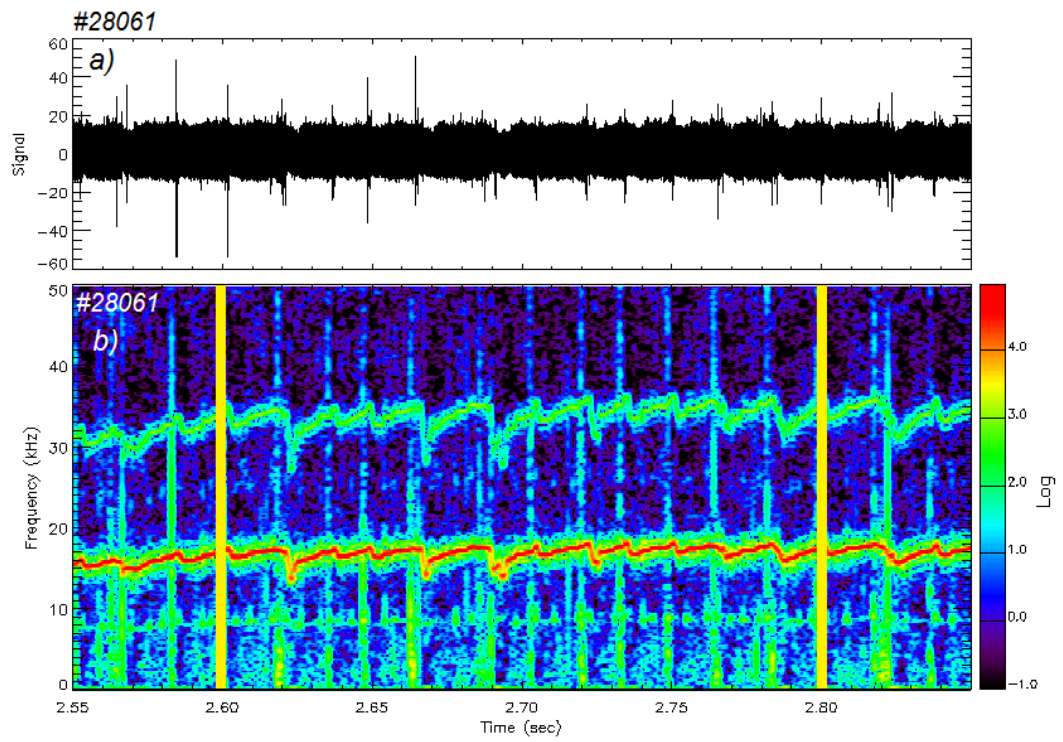


Figure 3.2.: a) Signal of B31-14 of AUG discharge #28061 from 2.55s to 2.85s b) spectrogram showing logarithm of the power spectral density of this signal

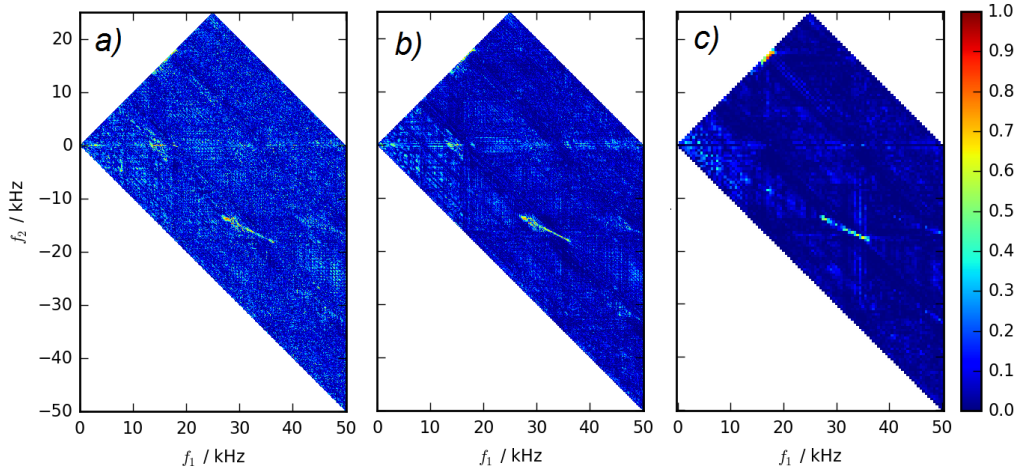


Figure 3.3.: Auto-bicoherence $BIC(f_1, f_2)$ of the Magnetic field fluctuation B31-14 from 2.6s to 2.8s. a) 10bins á 40 000 points, b) 20bins á 20 000 points, c) 100 bins á 4 000 points

different bin sizes where a) 10bins á 40 000 points, b) 20bins á 20 000 points and c) 100 bins á 4 000 points. As expected the frequency resolution decreases when shrinking the bins, but the noise is reduced when increasing the number of bins. To increase the detection level a Hann window was applied to the signal. The result can be seen in figure 3.4, where a) represents the auto-bicoherence of the signal split into 100 bins + Hann window, b) 200bins + Hann window and c) 100 bins with random noise with the same magnitude as the signal added. Figure 3.4a) shows the positive effect of windowing, where compared to figure 3.3c) the important features of the bicoherence become more prominent. However, as can be seen in figure 3.4b) the Hann window, having a low frequency itself, can also lead to points in the bicoherence suggesting coupling with low frequencies where there is no coupling. The addition of random noise to the measured signal leads to a decrease in noise in the auto-bicoherence picture (compare 3.3c) and 3.4c)), but lowers the overall intensity.

Figures 3.3 and 3.4 show, that the bicoherence algorithm works as expected for experimental data, and can detect the coupling of the mode with $f \approx 16kHz$ to its first harmonic with $f \approx 32kHz$.

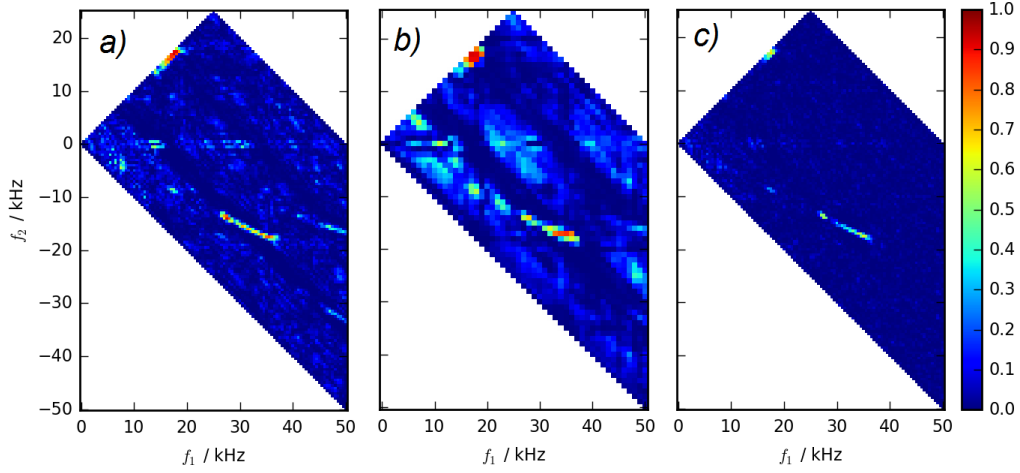


Figure 3.4.: Auto-bicoherence $BIC(f_1, f_2)$ of the Magnetic field fluctuation B31-14 from 2.6s to 2.8s. a) 100bins á 4000 points with applied Hann window, b) 200bins á 2000 points with applied Hann window, c) 100 bins á 4000 points with random noise added to the signal.

3.3. Conditional Average: ELM-Synchronizing

A problem in analyzing ELM related data is their **quasi** periodic structure. One can define an ELM frequency f_{ELM} but there is an uncertainty in the length of the inter ELM period.

To increase the statistical ensembles in ELM property analyses, data is synchronized at the ELM onset time. An example of this synchronization process is shown in figure 3.5 for the electron density n_e and temperature T_e of AUG discharge #30701. [25]

ELM onset times are determined from the inner divertor signal (red lines in figure 3.5a)). All signals of interest are then plotted on top of each other with respect to the ELM onset times as shown in 3.5b). These onsets times t_{ELM} , of AUG discharges, were previously determined by D_α light or the divertor current. To increase accuracy Mink [24] created an algorithm that roughly determines the vicinity of the ELM onset from the divertor signal and determines the real ELM onset from the flanks of the magnetic pickup coil signals. Magnetic signals synchronized with this technique were then analyzed with the bicoherence algorithm.

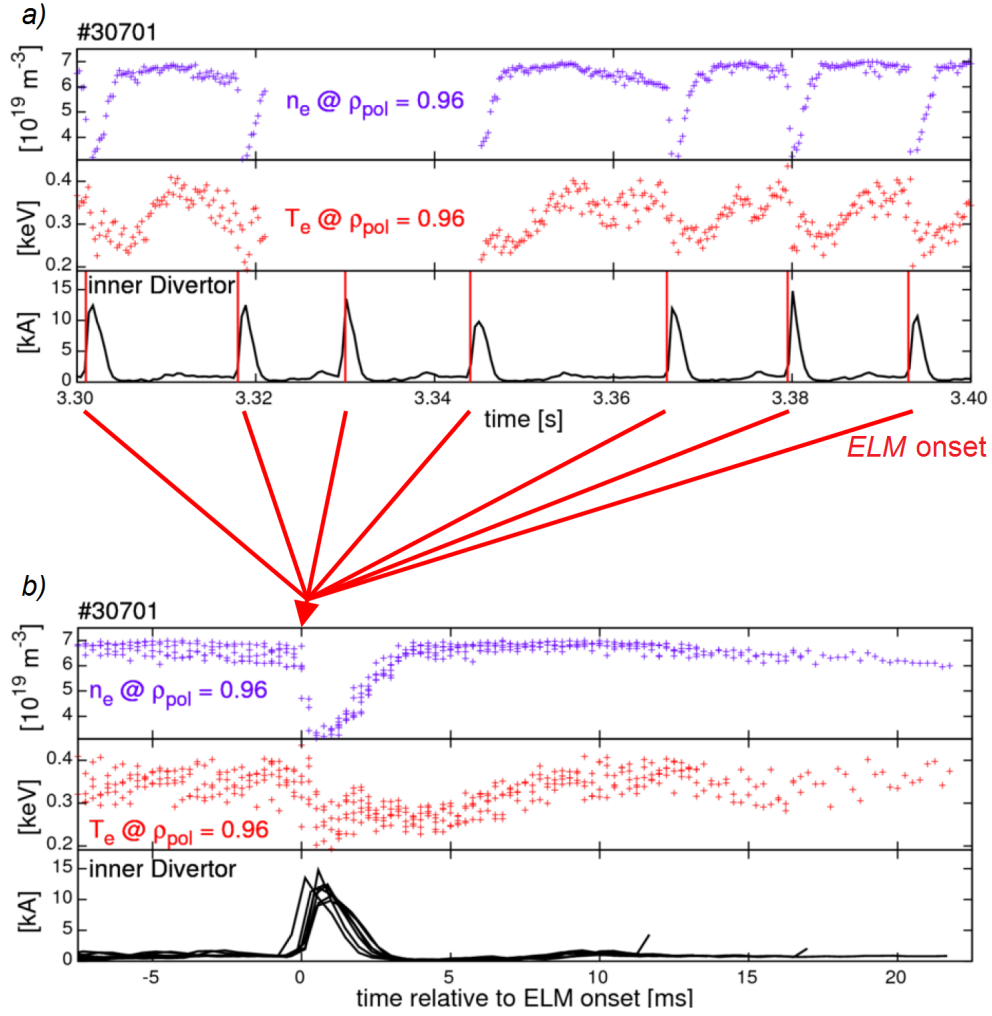


Figure 3.5.: Process of ELM synchronization via the divertor current. a) density and temperature profiles of discharge #30701 b) ELM synchronized signals [25]

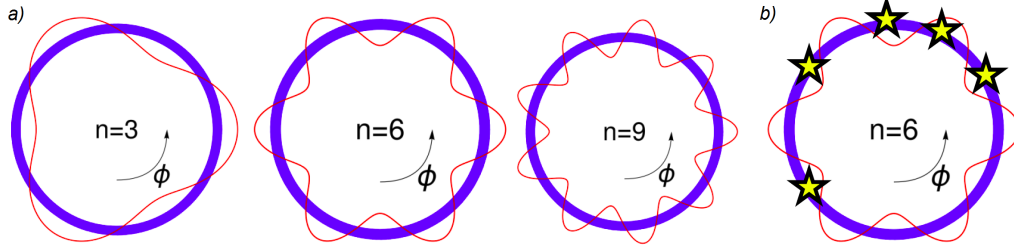


Figure 3.6.: Simple model of a toroidal fluctuation a) comparison of different mode numbers, b) position of magnetic coils (stars) picking up the fluctuation signal. [26]

3.4. Mode Number Determination

As discussed in chapter 1.3, plasma fluctuations can be decomposed into their Fourier modes. A sketch of toroidal fluctuations with different mode numbers can be seen in figure 3.6.

A method to determine these mode numbers is described in this section.

The phase $\varphi(f)$ of Fourier transformed periodic signals measured at different spacial positions contains information about the number of maxima, minima and zero crossings contained in the signal. It is therefore possible to determine the mode numbers of plasma fluctuations from such measurements.

A common method to do that, is to determine the phase $\varphi_i(f)$ of all measurements relative to one distinct reference measurement $\varphi_1(f)$ and plot it over the spatial position. The mode number for every frequency can then be computed as the slope of the ideal least squares fitted line. Since the calculated phase of a complex number is always in a range of $\varphi = [-\pi, \pi)$, phase shifts of $\Delta\varphi = k(\pm 2\pi)$ have to be allowed to be able to detect mode numbers $|n| \geq 2$.

In summary the mode-number calculation works as follows:

- Start with i signals $x_i[t]$ measured at different (toroidal for n , and poloidal for m) positions.
- Fourier transform the signals: $X_i[f]$
- Compute the phase of the signals: $\varphi_i[f]$

1. Plot phase difference against the toroidal/poloidal position: $\varphi_i = \varphi_i[\phi_i]$

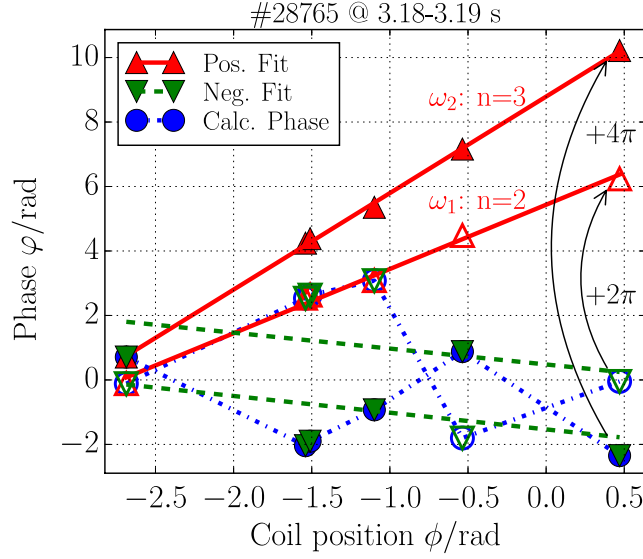


Figure 3.7.: Linear fits to the calculated phases $\varphi(f)$ allowing shifts of $\Delta\varphi = k(\pm 2\pi)$, $k \in \mathbb{N}$ for two $n = 2$ ($\omega_1 = 2\pi f_1$, open symbols) and $n = 3$ ($\omega_2 = 2\pi f_2$, closed symbols) modes measured by the six toroidally distributed pick-up coils at positions ϕ [24]

2. Perform least squares linear fit where uncertainties of $\pm k(2\pi)$, with $k \in \mathbb{N}$, are allowed for all φ_i with $i > 1$.
 3. Compute the slope of the fitted line: n
- Repeat steps 1-3 for every frequency: $n[f]$

Figure 3.7 shows an example of this fitting process for data taken from AUG discharge #28765. A 10ms time window starting at 3.18s, containing a $n = 2$ and a $n = 3$ mode (both rotating in co-current direction) is analyzed. The plot contains the measured phase differences of two frequencies representing the two modes. For the two rightmost points for ω_1 (open symbols) a phase shift of 2π was needed to get an ideal fit, while for ω_2 (closed symbols) 4 points needed a 2π shift and one point a 4π shift to get the ideal linear fit. Fits with negative mode numbers (rotating in counter-current direction) are also included in figure 3.7, but are not in agreement with the measured data.

To create a frequency resolved mode number histogram, this fitting process is repeated for all frequencies contained in the spectrum. *Mink et al.* used this

method to determine poloidal and toroidal mode numbers of magnetic fluctuations, by looking at signals of multiple pickup coils around the torus [24].

An example which shows the precision of the determination of toroidal mode numbers is given in Figure 3.8. The figure displays a time resolved frequency histogram (a). Such a histogram is created by choosing a time interval with constant plasma conditions (given on the top of the plot) and subdividing it into sub-intervals to show the temporal evolution. Spectra for all six toroidal pick-up coils are then calculated for all sub-intervals and binned together normalized to the maximum intensity. That is the reason why such plots are called frequency histograms and not spectra.

The plot in figure 3.8b) shows a frequency resolved mode number histogram. f resolved n/m histograms are created by again selecting a time range with constant plasma conditions (marked with white vertical lines in the frequency histogram, figure 3.8a)). This time window is then evaluated by the previously described linear fit method for each frequency, where the intensity is again the averaged intensity of all coils at the selected frequency. The histograms are normalized to the maximum intensity.

Figure 3.8c) shows the raw signal of one of the magnetic pick-up coils, reflecting the characteristic shape of the present mode, while figure 3.8d) displays the frequency integration of the $f[n]$ histogram, and therefore shares the mode number axis with the histogram.

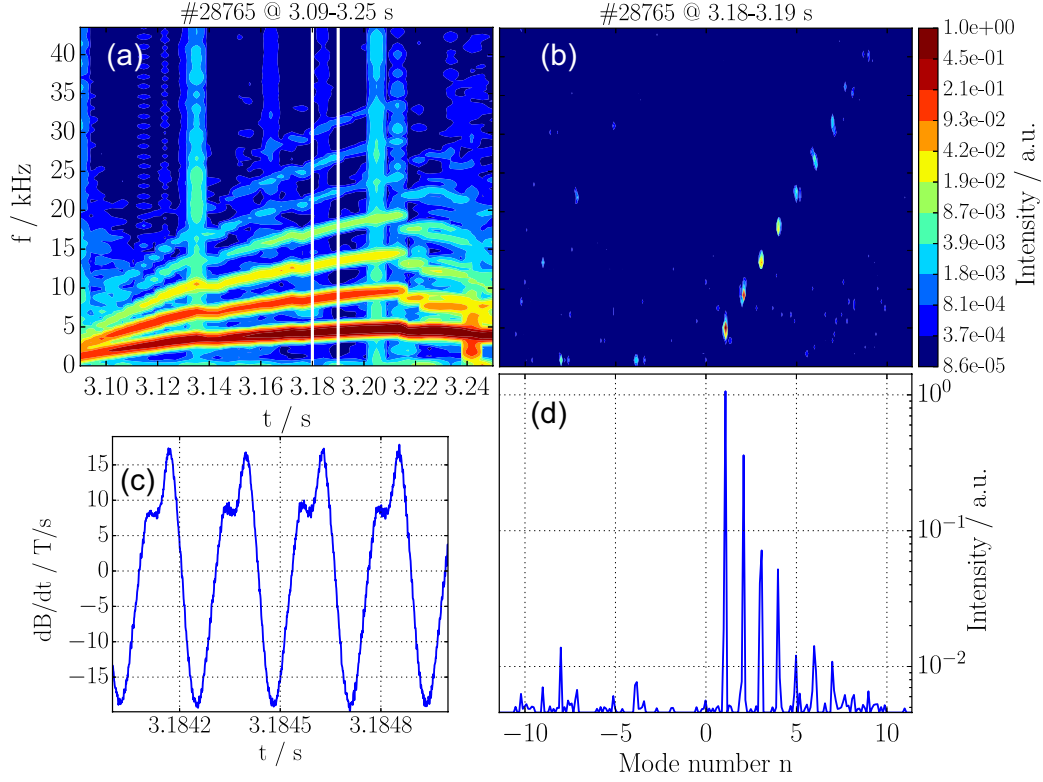


Figure 3.8.: (a) Time resolved frequency histogram, (b) frequency resolved mode number histogram, (c) magnetic signal of the B31-14 coil and (d) a frequency integrated mode number histogram for an $n=1$ core mode propagating in the co-current direction and its higher harmonics.[24]

To demonstrate the coupling of the $n = 1$ up to the $n = 7$ modes contained in pickup coil signal and shown in the frequency resolved mode number histogram 3.8b) the auto-bicoherence of the signal was computed. The line arrangement of the points in the modenumber histogram suggests that the modes most probably move with the same velocity $v \propto f/n$ and are therefore at the same radial position in the plasma.

It should again be emphasized that, applying a Hann window function creates intensities in the bicoherence, where the original data has none (compare figure 3.9a) and b)) and that dithering improves the resolution while decreasing detectability (compare figure 3.9a) and c)). The mode coupling structure is best displayed by the auto-bicoherence of the dithered and windowed signal 3.9d).

The points in the auto-bicoherence are arranged on lines with varying slopes representing coupling of modes to different harmonics. The Line with a -22.5° slope (bisecting the auto-bicoherence triangle with $f_2 < 0$) for example, represents the coupling of modes to themselves to create the first harmonics $n_2 + n_2 = 2n_2 = n_1$ (visible in the auto-bicoherence as $(f_1, f_2) = (5\text{kHz}, -2.5\text{kHz}), (10\text{kHz}, -5\text{kHz}), (15\text{kHz}, -7.5\text{kHz}), \dots$). Furthermore if the contained modes are all harmonics the three wave coupling condition will be fulfilled for different so-called mode coupling channels. Other examples are represented by the lines with -11.25° and -33.75° slope, where the three wave coupling condition is fulfilled as $n_2 + \frac{n_2}{2} = n_1$ or $n_2 + \frac{3n_2}{2} = n_1$. These mode coupling channels are highlighted in figure 3.10.

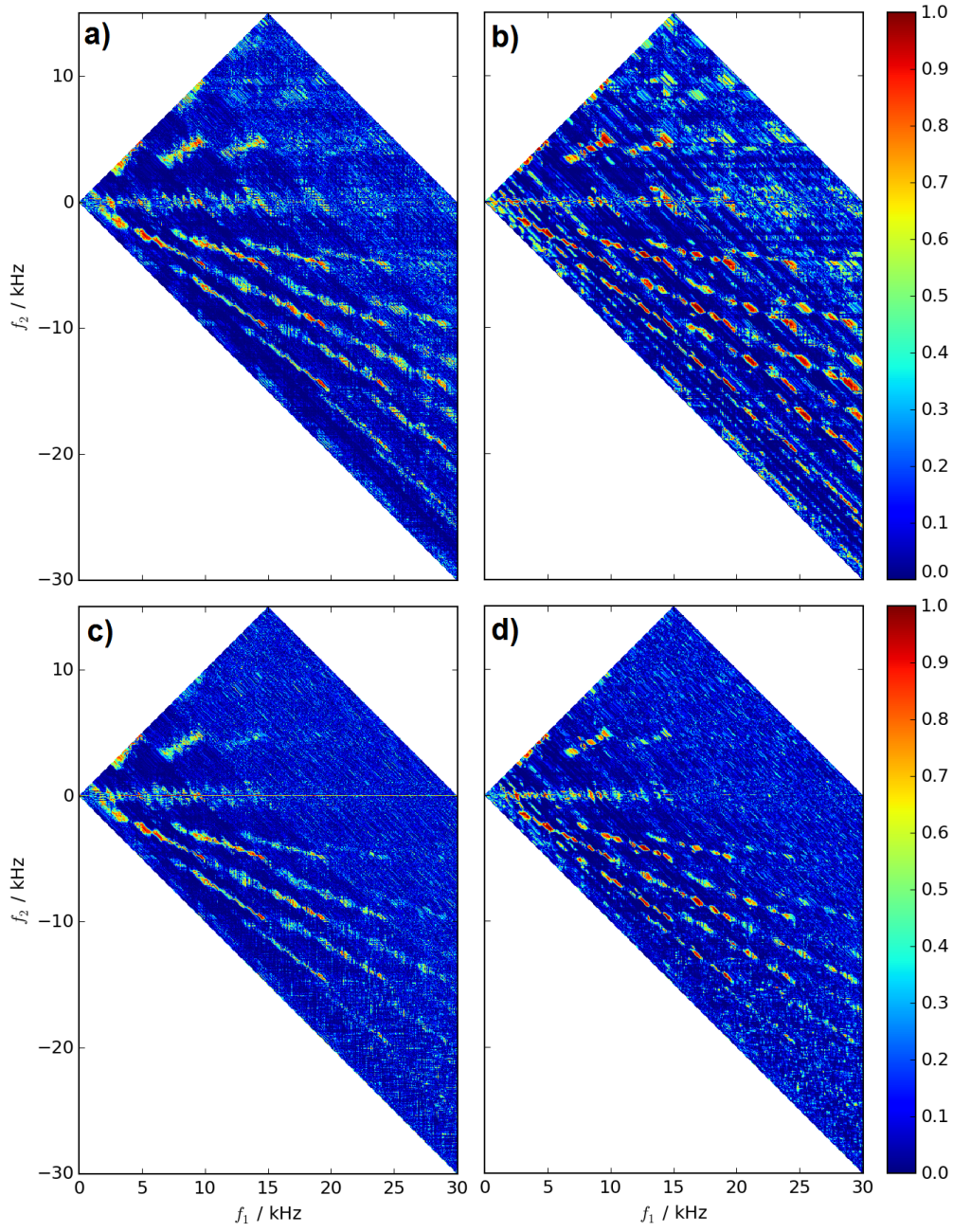


Figure 3.9.: Auto-bicoherence of pickup coil B31-14 signal from AUG discharge #28765 at 3.09 to 3.25s split into 10 equal sized bins, where a) is the unaltered signal, b) the signal with applied Hann window, c) the dithered signal (added gaussian noise with signal amplitude) and d) dithered and windowed signal.

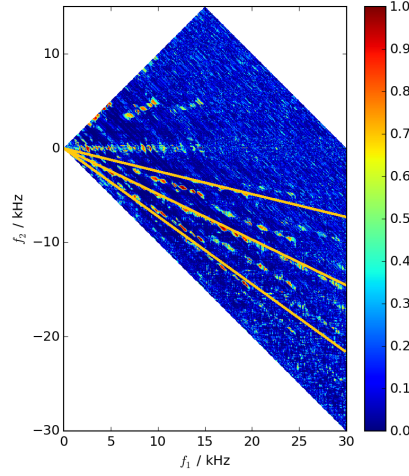


Figure 3.10.: Mode coupling channels of pick-up coil B31-14 signal from AUG discharge #28765 highlighted with orange lines.

3.5. Bicoherence of the ELM Cycle

To resolve different phases during the ELM cycle *Mink et al.* analyzed pick-up coil data of AUG discharge #28767 containing a stationary phase from 2.0s to 2.5s with 25 ELMs and a low ELM frequency of about $f_{ELM} \approx 50\text{Hz}$. Further parameters of this discharge are $I_P = 0.8\text{MA}$, $P_{Heat} = P_{NBI} + P_{ECRH} = 2.5 + 1.5\text{MW}$, $|B_t| = 2.5\text{T}$ and line integrated core electron density $n_e = 6.0 \cdot 10^{19}\text{m}^{-2}$. The time traces of the magnetic pick-up coil signal, the inner divertor shunt current, the ELM frequency, the plasma stored energy and the line averaged density at the core and the edge are shown in figure 3.11.

Following the process described in chapter 3.3 leads to ELM synchronized electron temperature T_e and density n_e profiles. Figure 3.12 displays that these profiles show distinct characteristics in different phases relative to the ELM onset time and can therefore be divided in six phases. Details on the classification of these so-called inter ELM phases would go beyond the framework of this thesis, but can be found in the literature [27, 28, 29, 12].

Spectral data of a typical ELM cycle can be seen in figure 3.13, showing a time resolved frequency histogram of B31-14 data from AUG discharge #28767 at 2.0s to 2.5s, with conditional averaging over 25 ELMs, in a time range from

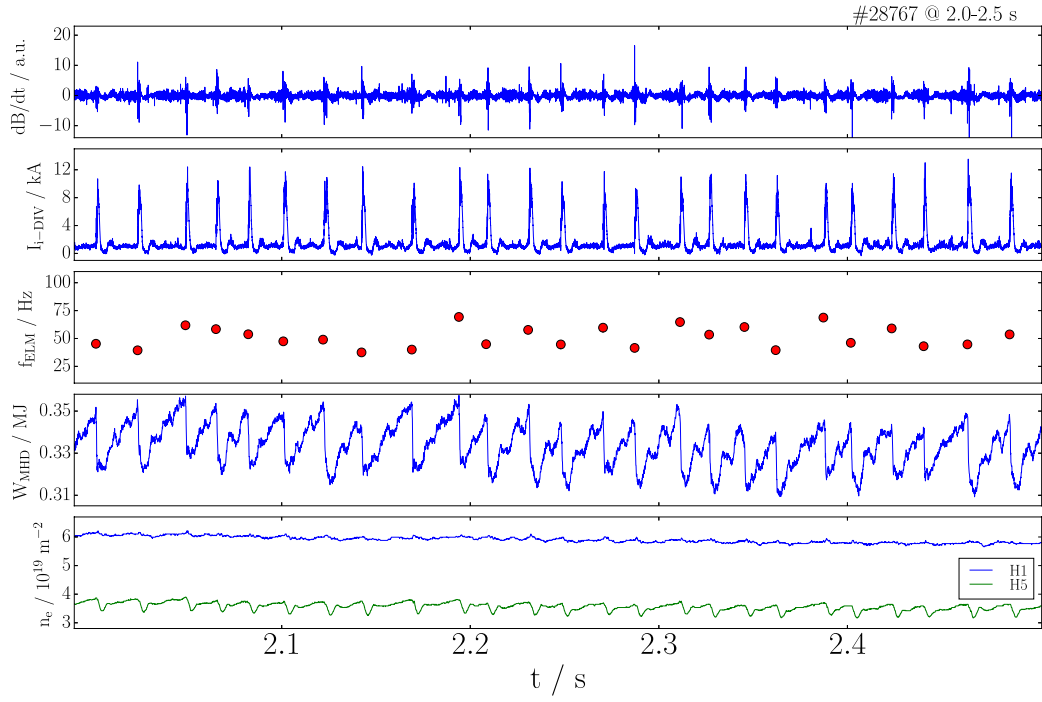


Figure 3.11.: Time trace of discharge #28767. Shown are the signals of the magnetic pick-up coil B31-14, the inner divertor shunt current, the ELM frequency, the stored energy calculated from the equilibrium and the line integrated density measured from two interferometry channels through the core (H1) and the edge (H5)[24]

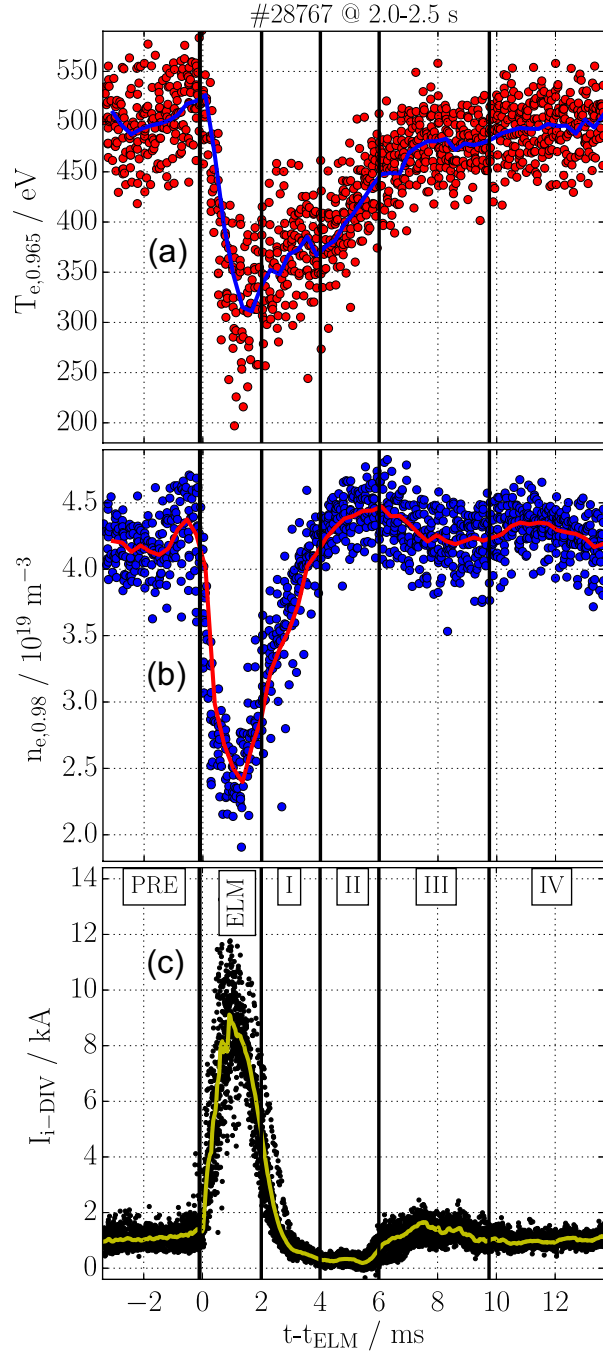


Figure 3.12.: ELM-synchronized data points of (a) the electron temperature T_e and (b) density n_e at the pedestal top ($\rho = 0.965$ and $\rho = 0.98$) evaluated with the integrated data analysis tool IDA and (c) the inner divertor shunt current as a measure for the transport over the separatrix together with the smoothed signal of all quantities.[24]

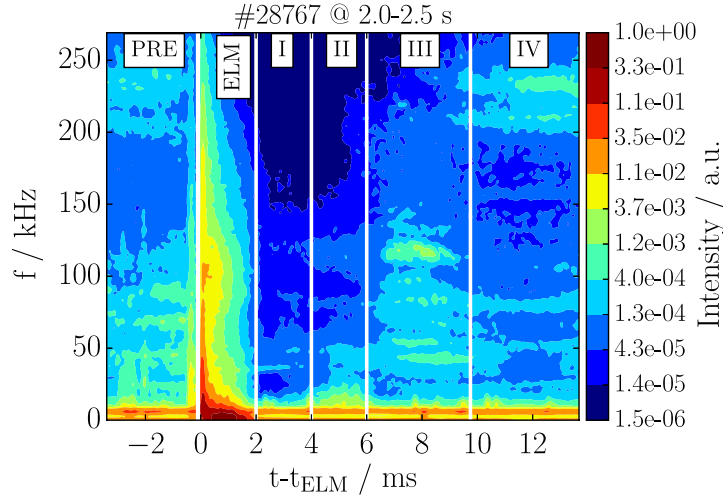


Figure 3.13.: Time resolved frequency histogram of B31-14 data from AUG discharge #28767 at 2.0s to 2.5s in a time range from 4ms before the ELM onset to 14ms after showing the six distinct ELM phases. [24]

4ms before the ELM onset to 14ms after. The six ELM phases exhibit various spectral characteristics. It is therefore reasonable to check the auto-bicoherences of the phases in detail.

3.5.1. PRE - ELM Phase and Phase IV

The time range from $t - t_{ELM} = -2\text{ms}$ to $t - t_{ELM} = 0\text{ms}$ (ELM onset time) is called the pre-ELM (PRE in figure 3.13) phase and has the most interesting properties from a spectroscopic perspective. It shows high intensities for 2 different frequency bands: $10\text{kHz} < f < 100\text{kHz}$ and $200\text{kHz} < f < 250\text{kHz}$ with a gap with much lower intensities between those bands. A mode number analysis (see red arrows in figure 3.14) showed that these two modes represent the toroidal mode numbers $n = -3, -4, -5$, and $n = -9, -10$ rotating in counter current direction. Looking back at the previous chapters one could expect a coupling between those bands to be visible in the auto-bicoherence of this phase.

To improve statistics the considered timewindow was increased to reach from 2.0s to 3.5s containing 71 ELMs, while retaining a relatively stable ELM frequency and comparable magnetic properties. Figure 3.15a) shows the auto-bicoherence of the magnetic signal picked up by the B31-14 coil from 2.0s to 3.5s. The data was

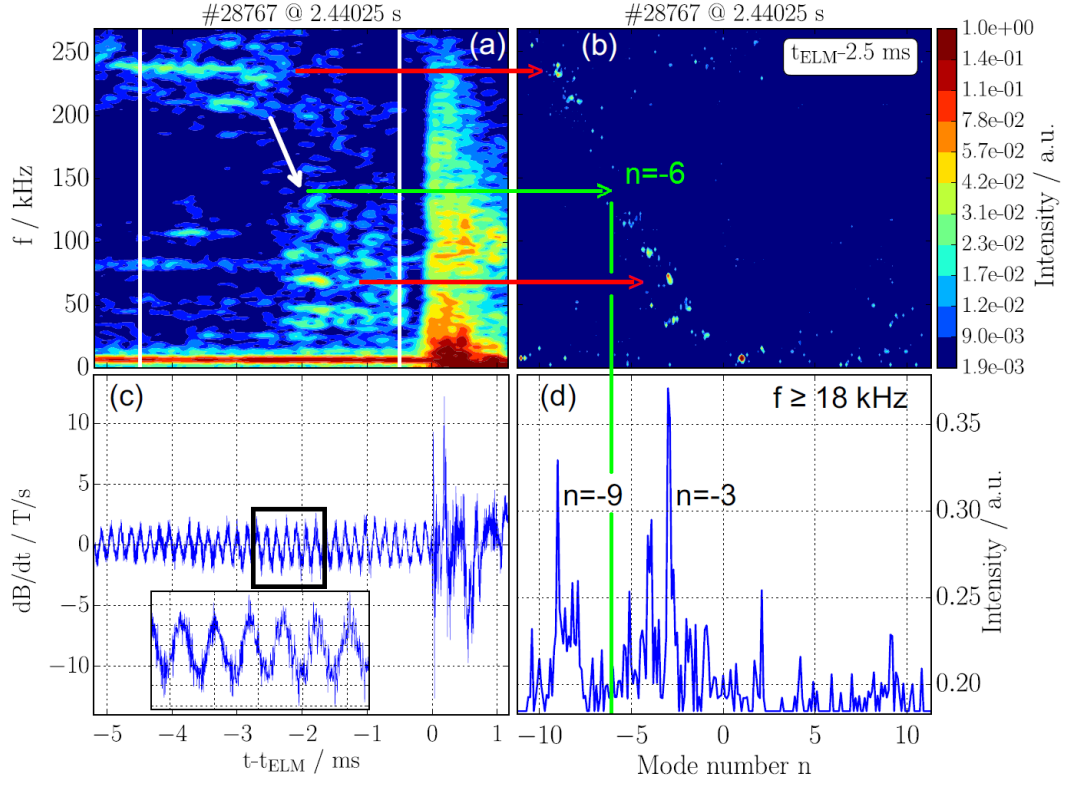


Figure 3.14.: (a) Frequency histogram synchronized to one single ELM at 2.44 s. A jump in the evaluated frame (marked with white stripes) from high frequencies to low frequencies is illustrated by the white arrow (b) Mode number resolved frequency histogram and (d) mode number histogram integrated over frequencies above 18 kHz of a 4 ms time window around 2.5 ms before one characteristic ELM onset. (c) The magnetic raw signal of the analyzed time frame together with a zoom around 2.2 ms before the ELM. The green arrows emphasize the non existence of a peak at $n = -6$. [24]

ELM synchronized using the method described in chapter 3.3 and $BIC(f_1, f_2)$ was computed for a time interval from 1.5ms to 0.1ms before the ELM. Instead of the expected point couplings of the 2 frequency bands, line structures are visible at $f_1 + f_2 < 20\text{kHz}$ and $f_1 + f_2 \approx 150\text{kHz}$. These diagonal lines in the bicoherence suggest that the three-wave-coupling condition is satisfied for any frequency pairs (f_1, f_2) where the sum frequency $f = f_1 + f_2$ is constant. Even though the spectral intensity of the preELM phase at $f = 150\text{kHz}$ seen in figure 3.13 is very low compared to the intensities of the low and the high frequency band, the bicoherence shows a line at $f_1 + f_2 \approx 150\text{kHz}$.

This phenomenon might be described by a so called Virtual Catalytic Mode (VCM), that is not visible in the power-spectrum but in the bicoherence. It couples the low and the high frequency band non-linearly, without having a lot of spectral energy itself. A mode number analysis, depicted in figure 3.14, showed that 150kHz represents a $n = -6$ mode. This $n = -6$ mode would fulfill the three wave coupling condition and connect the $n = -3, -4$ and the $n = -9, -10$ frequency bands.

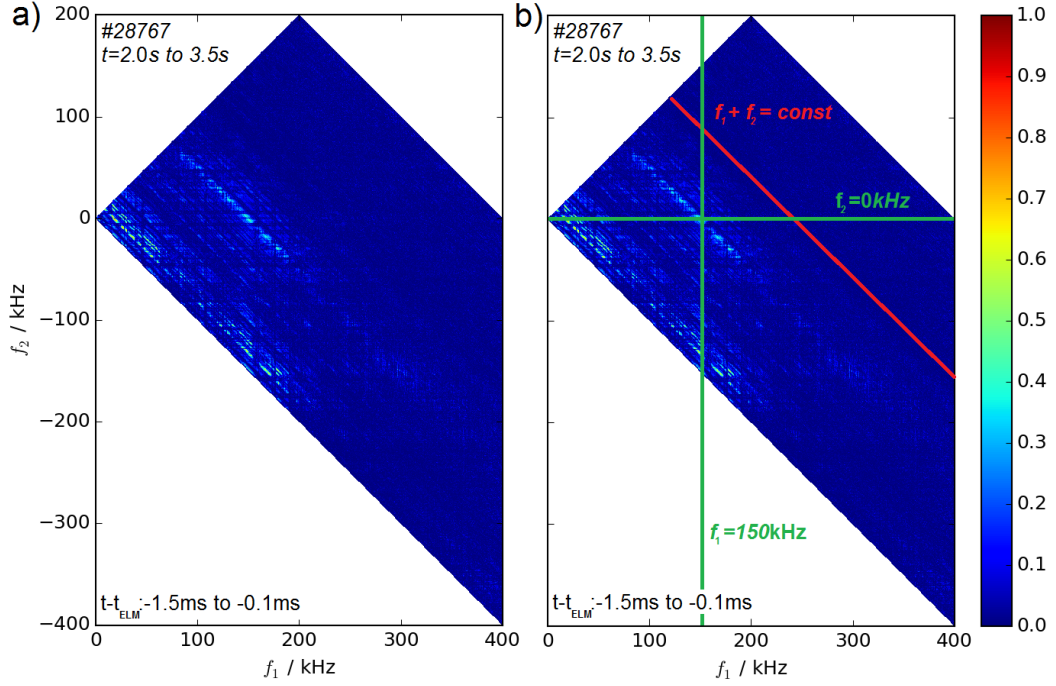


Figure 3.15.: a) Auto-bicoherence of the pre-ELM phase ($t - t_{ELM} = -1.5\text{ms}$ to -0.1ms) ELM synchronized signal from B31-14 of AUG discharge #28767 at 2.0s to 3.5s (73 ELMs) and b) where the red line and its parallels represent the condition $f_1 + f_2 = \text{const}$ and the green lines mark a point of strong bicoherence.

Taking a closer look at the spectrum of the preELM phase it was found, that there is indeed spectral intensity at $f = 150 \text{ kHz}$, at about 0.3ms before the ELM onset. To determine if this preELM structure is a singular event or is present in every ELM the power spectrum was computed for nested intervals between 2.0s and 3.5s. It was found, that this 150kHz structure was restricted to a time between 2s and 2.11s by analyzing the spectrum of the magnetic signal using a nested intervals approach. The 2.0s and 3.5s time frame was split in half to check if the 150kHz intensity occurs before or after 2.75s or both. This process was repeated until it was found, that the ELMs occurring at 2.06546s and 2.10103s are the ones causing the 150kHz pre-ELM intensity.

The power-spectra of those ELMs are depicted in figure 3.16. They show a double peak spectral structure, where the ELM synchronization has set the ELM onset at the second peak (see $t - t_{ELM} = 0$).

Figure 3.17 shows detailed time traces of the time frame around the 2.10103s

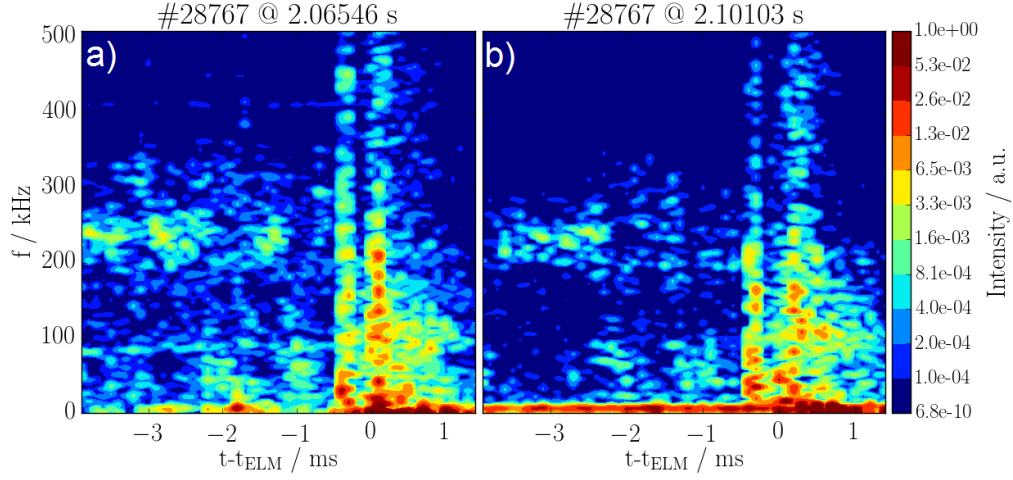


Figure 3.16.: Double peak structure in the power-spectra of magnetic signals #28767 B31-14 for ELM at a) 2.06546s and b) 2.10103s

ELM. The magnetic signals $\frac{dB}{dt}$ in figure 3.17a) and $\frac{d^2B}{dt^2}$ in figure 3.17b) show the pre-ELM fluctuations that lead to the double peak spectral structure, while the divertor current only shows a slight shoulder-like increase before the big peak occurs.

It was found in further bicoherence analyses, that the line structure disappeared when the two mentioned ELMs were not included in the time windows. This shows that the auto-bicoherence is very sensitive to the selection of ELMs. If an ELM with a double peak spectral structure is contained in the analyzed data and the ELM synchronization sets t_{ELM} at the start of the second peak the first peak will be visible in the bicoherence as a line structure in the pre-ELM phase.

Because of the periodic structure of the ELM cycle, similar characteristics as described for the pre-ELM phase also apply to Phase IV, where the bicoherence line at $f_1 + f_2 = 150\text{kHz}$ of AUG discharge #28767 at 2.0s to 3.5s reappears at $t - t_{ELM} = 16\text{ms}$.

3.5.2. ELM Phase

At the ELM onset line structure at $f_1 + f_2 = 150\text{kHz}$, created by the double peak ELMs, disappears and the autobicoherence flickers for up to $100\mu\text{s}$. Figure 3.18

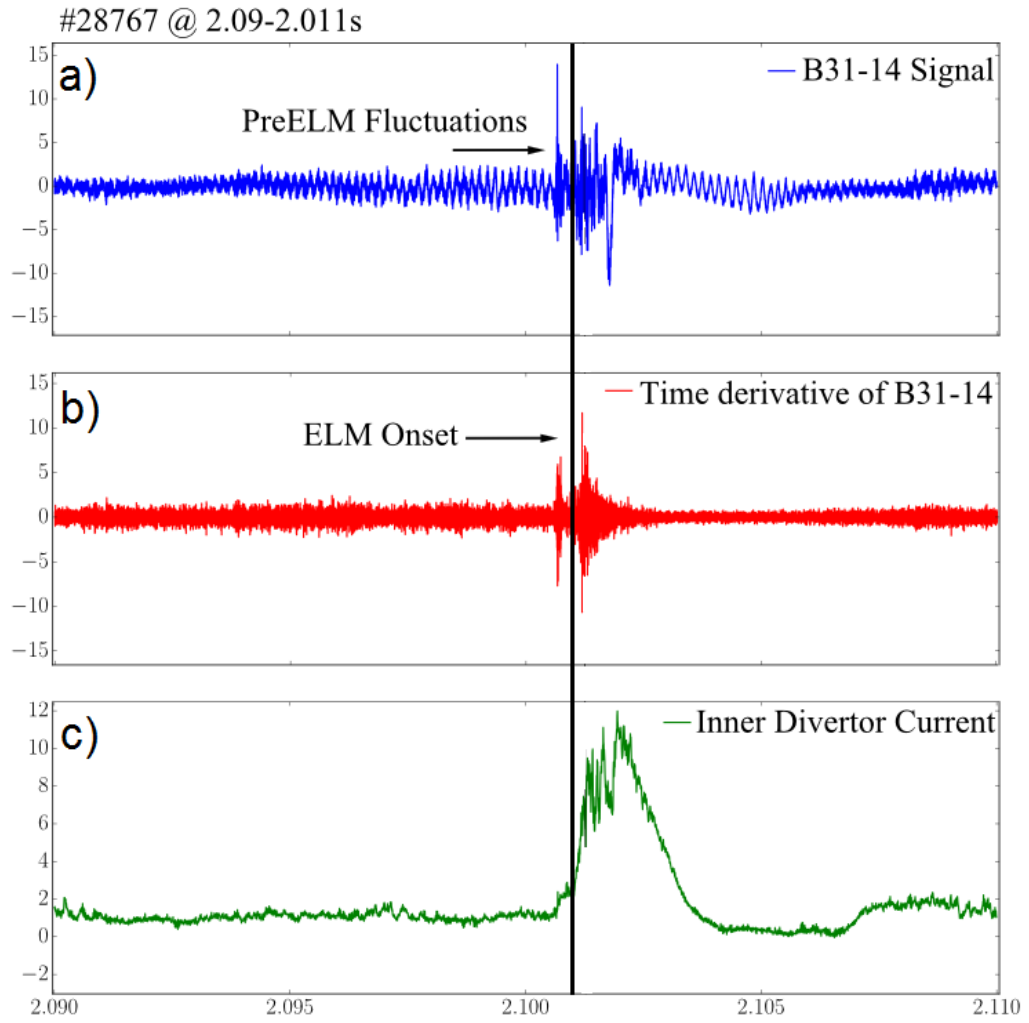


Figure 3.17.: Time traces of AUG discharge #28767 in the vicinity of the ELM at 2.101s where
a) pick-up coil B31-14 signal b) the time derivative of the pick-up coil signal and
c) the inner divertor current.

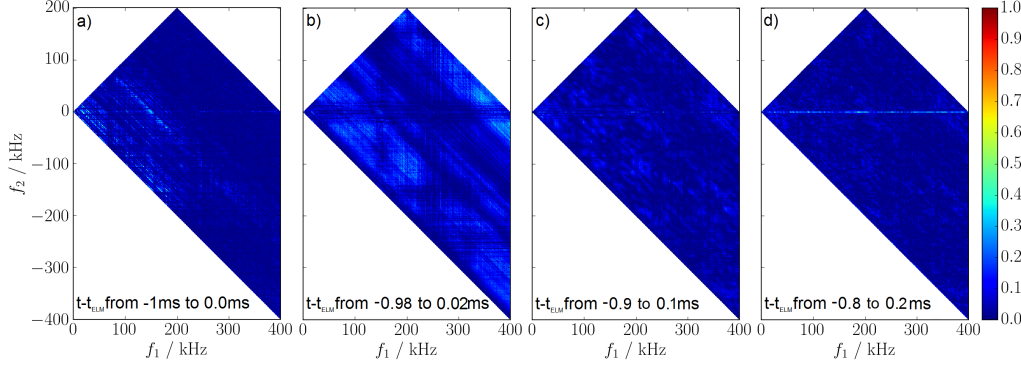


Figure 3.18.: Auto-bicoherence of ELM synchronized magnetic signals from AUG discharge #28767 at 2.0s to 3.5s of the ELM phase a) time window from $t - t_{ELM} = -1\text{ms}$ to 0ms, b) from -0.98ms to 0.02ms , c) from -0.9ms to 0.1ms and d) from -0.8ms to 0.2ms .

shows the auto-bicoherence of time frames shifted across the ELM onset. While the line structure at $f_1 + f_2 = 150\text{kHz}$ can still be seen in figure 3.18a), in which the analyzed window is -1ms to 0ms before the ELM, figure 3.18b) (with a window from -0.98ms to 0.02ms) already shows the mentioned broadband flickering. This happens, because the ELM itself has a very high intensity broadband frequency distribution as can be seen in the spectrum given in figure 3.13. The three-wave-coupling condition is therefore met for nearly every frequency contained in the spectrum. It was found that this flickering in the bicoherence happens, as mentioned before, on a sub-millisecond ($20 - 100\mu\text{s}$) time scale. Figure 3.13c) still shows some of the ELM flickering, but with decreasing intensity. After $200\mu\text{s}$, figure 3.13d) the auto-bicoherence of the magnetic signal quiets down again and only shows some coupling of the spectrum to very small frequencies. This also happens in Phase I-III and is described in the next section.

3.5.3. Phase I-III

The power-spectrum of these phases, especially in phase III (see figure 3.13) suggests the presence of strong magnetic modes. Bicoherence analysis, seen in figure 3.19 which shows the power spectrum of the ELM synchronized B31-14 signal from AUG discharge #28767 at 2.0s to 3.5s and the auto-bicoherence of phase III ($t - t_{ELM}$ ranging from 7ms to 9ms after the ELM) of this signal, shows

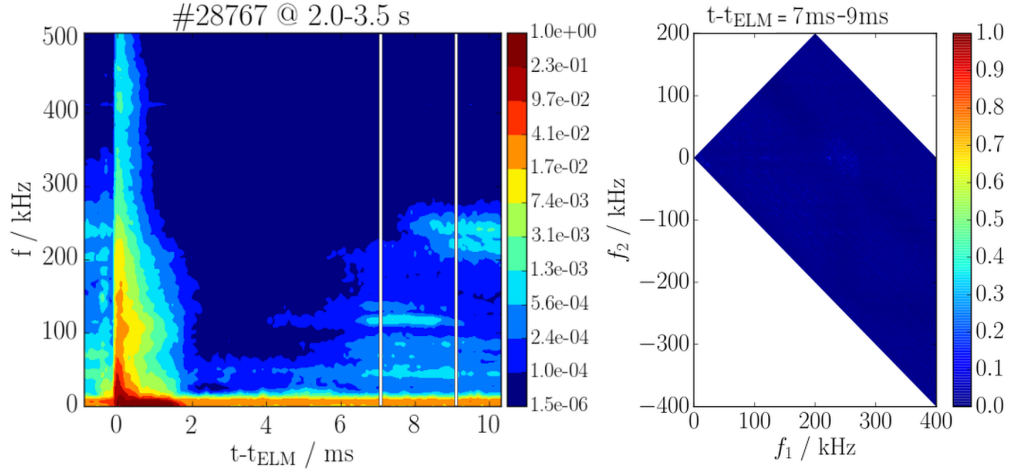


Figure 3.19.: Search for mode coupling in phase III with a) ELM synchronized power-spectrum of B31-14 signal from AUG discharge #28762 at 2.0s to 3.5s and b) auto-bicoherence of the signal from $t - t_{ELM}$ ranging from 7ms to 9ms after the ELM.

no apparent mode coupling. In Phase I and Phase II there is an occasional line at $f_2 = 0$, visible in the bicoherence, similar to figure 3.18d), which suggests couplings with the DC part of the signal. The fact that the mean of the signal is subtracted for every bin prevents the signals from having a DC part, therefore the coupling has to come from frequencies below the frequency resolution, which is 1kHz for 1ms time windows. The time ranges of Phase I-III were analyzed with window sizes of up to 8ms ranging from 2ms to 10 ms after the ELM covering all three phases. The big problem of increasing the window size is, that while the frequency resolution improves, the time resolution is decreased, because more data is being analyzed. Even with the therefore improved frequency resolution to $\Delta f = 125\text{Hz}$ the line structure at $f_2 = 0$, present in Phase I and II was still found in the bicoherence. The fact that these low frequencies couple to the broad band of frequencies in the spectrum, or how this happens, could not be described in a proper scientific way, because the frequency resolution is too low.

4. Conclusions

As shown in the many examples above the autobicoherence is a valuable tool to detect non-linear effects such as mode coupling. To deliver a good overview, all insights gained in the course of this thesis are summarized in this chapter. Further research opportunities are compiled in the last section.

4.1. Summary

Over the course of this thesis an analytical quadratic mode coupling model was proposed and an algorithm that computes the auto-bicoherence of any given times series was created to test this model. This algorithm was then thoroughly tested and it was found, that adding random noise and applying a Hann window function to the time signal can improve detectability, but can also lead to numerical artefacts. These so-called windowing and dithering methods therefore have to be used with caution.

The tested bicoherence algorithm was then used to analyze data obtained from magnetic pick-up coils signals of ASDEX Upgrade discharges. Looking at data from AUG discharge #28061 it was found, that coupling of a plasma mode to its first harmonic can be seen in the auto-bicoherence.

With the mode number determination technique used by *Mink et al.* it was demonstrated, that if a signal contains many magnetic modes, different coupling channels can be seen in the auto-bicoherence. These mode coupling channels of the pick-up coil signal from AUG discharge #28765 can be seen in figure 3.10.

Furthermore, the auto-bicoherence was used to check for couplings in ELM synchronized data. To avoid interference of disturbing effects an ASDEX Upgrade discharge (#28767) with a nearly stationary phase from 2.0s to 3.5s containing 71

ELMs with low ELM frequency of about $f_{ELM} = 50Hz$ was chosen, the magnetic signals ELM synchronized and divided into six distinct phases.

A $f_1 + f_2 = 150kHz$ line structure (figure 3.15) was found in the pre-ELM phase of the B31-14 pick-up coil signal and was first explained by a Virtual Catalytic Mode (VCM), see section 3.5.1. To examine the existence of the proposed Virtual Catalytic Mode in the preELM phase many discharges with varying properties were analyzed. Looking at first analyzed data, it was suspected, that the proposed mode depended on the frequency of the high intensity low frequency mode visible in all magnetic power spectra, called the core mode. Therefore discharges with different core mode frequencies were selected. Another idea was that the presence of neoclassical tearing modes, could alter the VCM frequency. To improve the time resolution and to display the temporal evolution of the coupling data, the auto-bicoherence was computed for many time windows.

The 1ms time window for the pre-ELM phase analysis started at $t - t_{ELM} = -2.5ms$ to $-1.5ms$, where the bicoherence was computed and plotted. It was then shifted by $10\mu s$ to $t - t_{ELM} = -2.49ms$ to $-1.49ms$ where the bicoherence was calculated and plotted again. This process was repeated until the window reached the ELM at $t - t_{ELM} = 0ms$ to $+1ms$. One pre-ELM phase analysis therefore created 250 bicoherence plots. To manage such a big amount of data, videos were created that displayed the temporal evolution of the bicoherence in the pre-ELM phase. The flickering in the bicoherence of the ELM phase described in section 3.5.2 was the only distinct characteristic that was visible in the videos of all analyzed discharges.

Further analysis of single ELM spectra showed that the proposed VCM was not really a mode, but an artefact produced by ELMs that display a double peak spectral structure and are synchronized at the second peak. As with windowing and dithering one has to be very careful with the ELM synchronization and the selection of the ELMs to represent what is really going on in the ELM Cycle from a mode coupling perspective.

Except for a non resolvable line at $f_2 = 0$, the auto-bicoherence of phases I-III of the magnetic signal from AUG discharge #28767 and all other analyzed discharges displayed no apparent mode coupling.

All in all no evidence for simple mode coupling, meaning no clearly visible

structure, was found in the analyses of the different ELM phases.

4.2. Outlook

In bispectral analysis the definition of the auto-bispectrum can be generalized to the cross-bispectrum

$$B_{XY}(f_1, f_2) = X(f_1)X(f_2)Y(f_1 + f_2)^* \quad (4.1)$$

and the auto-bicoherence to the cross-bicoherence

$$CBIC(f_1, f_2) = \frac{\langle |B_{XY}(f_1, f_2)| \rangle^2}{\langle |Y(f_1 + f_2)|^2 \rangle \langle |X(f_1)X(f_2)|^2 \rangle}. \quad (4.2)$$

The cross-bicoherence of two different magnetic coils could be used in future work to analyze mode coupling with spatial resolution.

Ritz et al. and *Kim et al.* suggested different algorithms that make it possible to calculate the spectral energy transfer between coupled modes using auto- and cross-bicoherences[30, 31]. The implementation of these algorithms could be very interesting for future work.

A. Danksagung

Beschließen möchte ich diese Arbeit und somit einen großen Lebensabschnitt, damit einmal Danke zu sagen.

Zu allererst geht mein Dank an meinen Betreuer in Wien, *Friedrich Aumayr*, dessen Management Fähigkeiten mich jeden Montag aufs Neue beeindruckten und dessen Leitung die Arbeitsgruppe erst zu der wissenschaftlichen Familie macht, die sie ist. Danke für die finanzielle und auch wissenschaftliche Unterstützung.

Ein sehr großes Dankeschön geht an meine Betreuerin in Garching, *Elisabeth Wolfrum*, deren Vorlesung mein Interesse an der Plasmaphysik geweckt hat und die mich nicht nur in physikalischen Problemstellungen immer bestens beraten hat. Deine Neugierde und deine Freude über neu gewonnene Erkenntnisse waren und sind eine große Inspiration.

Vielen Dank auch an *Peter Manz*, der mir den Einstieg in die Entschlüsselung der Geheimnisse der Bikohärenz enorm vereinfacht hat und mir die auch noch so grundlegenden Fragen und Probleme so oft erklärt hat, bis auch mir ein Licht aufging.

Am meisten Zeit hat, nach mir, wahrscheinlich *Felician Mink* mit dieser Arbeit verbracht. Danke, dass du dir so wahnsinnig viel Zeit genommen hast mir ein guter Betreuer zu sein und mir zu jeder Tages- und Nachtzeit immer konstruktive Kritik und wertvolles Feedback geliefert hast.

Danke auch an *Florian Laggner*, der mit seinem tiefen Wissen in der Plasmaphysik und seiner offenen lustigen Art immer ein Vorbild für mich sein wird. Ich werde versuchen, deine großen Fußstapfen so gut wie möglich auszufüllen.

Auch meine Garchinger und Münchner Kollegen und Freunde seien hier erwähnt. Speziell *Jakob, Marco, Matthias, Maxi, Michi, Sebastian* und *Stephan*, die die Aufenthalte in Deutschland immer wieder zu lustigen Erlebnissen gemacht haben und an so manchem Abend mit mir über Plasmaphysik und vieles mehr

philosophiert haben.

Großer Dank gilt auch allen Kollegen der Arbeitsgruppe für Atom und Plasma-physik in Wien. Allen voran *Bernhard*, *Elisabeth* und *Richard*, von denen ich vieles über wissenschaftliches Arbeiten gelernt habe. *Janine* und *Reinhard*, die mich im Prozess des Schreibens mit ihren Erfahrungen unterstützt haben. *Bernd*, *Christian*, *David*, *Dominic*, und *Paul* durch die sich die Arbeit nicht wie die eines Einzelkämpfers anfühlte. Meinen Bürokollegen *Hakan*, (Danke für die Hilfe bei der Farbenwahl in figure 3.10) *Lukas* und *Rimpei*, die immer für ein nettes Arbeitsklima gesorgt haben. Danke für die vielen aufschlussreichen Gespräche bei Mittags- und Kaffeepausen.

Dankeschön auch an die Mitglieder des *Physiker Quaddro*: *Bene*, *Coco* und *Jo*. Ich bin froh euch zu meinen besten Freunden zählen zu dürfen.

Mein Dank geht auch an all meine Langauer Freunde, die mich schon vor dem Bachelor im Doktorat gesehen haben und mich, wenn ich wieder mal zu theoretisch oder verrückt werde, immer wieder auf den Boden der Tatsachen zurückholen.

Ein großes Dankeschön geht an *Magdalena*. Danke, dass du mir, besonders in der letzten stressigen Zeit, mit viel Geduld und Liebe zur Seite gestanden bist, auch wenn ich dir zum hundertsten Mal mit einem Problem bei dieser Abbildung oder jenem Abschnitt, ein Ohr abgekaut habe. Du gibst mir die Stabilität, die meine Zerstreuung in Grenzen hält.

Zu guter Letzt möchte ich mich bei meinem Papa *Friedrich* und meiner Mama *Herta Harrer* bedanken, die meine Neugier und Kreativität immer gefördert haben und mich in all meinen Vorhaben unterstützen. Danke dass ihr immer für mich da seid.

B. Bibliography

- [1] Stroth, U. *Plasmaphysik*; Vieweg+Teubner Verlag, 2011.
- [2] Eddington, A. *The internal constitution of the stars*; University Press Cambridge, 1926; pp viii, 407 p.
- [3] Wikimedia Commons, Fusion Reactionrate on 2016.10.19. https://en.wikipedia.org/wiki/Fusion_power.
- [4] Wikimedia Commons, Fusion Tripleproduct on 2016.10.19. https://en.wikipedia.org/wiki/Lawson_criterion.
- [5] Lawson, J. D. *Proceedings of the Physical Society. Section B* **1957**, *70*, 6.
- [6] Wesson, J.; Campbell, D. *Tokamaks*; International Series of Monographs on Physics; OUP Oxford, 2011.
- [7] Willensdorfer, M. Temporal behavior of the plasma edge density throughout the L-H transition in ASDEX Upgrade. Ph.D. thesis, TU Wien, 2013.
- [8] Wagner, F. et al. *Phys. Rev. Lett.* **1982**, *49*, 1408–1412.
- [9] Wolfrum, E.; Viezzer, E.; Burckhart, A.; Dunne, M.; Schneider, P.; Willensdorfer, M.; Fable, E.; Fischer, R.; Hatch, D.; Jenko, F.; Kurzan, B.; Manz, P.; Rathgeber, S.; the ASDEX Upgrade Team, *Nuclear Fusion* **2015**, *55*, 053017.
- [10] Connor, J.; Kirk, A.; Wilson, H. *AIP Conference Proceedings* **2008**, *1013*, 174–190.
- [11] Zohm, H. *Plasma Physics and Controlled Fusion* **1996**, *38*, 105.

- [12] Laggner, F. M. et al. *Plasma Physics and Controlled Fusion* **2016**, *58*, 065005.
- [13] Hölzl, M.; Merkel, P.; Huysmans, G.; Nardon, E.; Strumberger, E.; McAdams, R.; Chapman, I.; Günter, S.; Lackner, K. *Journal of Physics: Conference Series* **2012**, *401*, 012010.
- [14] Krebs, I. Non-Linear reduced MHD Simulations of Edge-Localized Modes in Realistic ASDEX Upgrade Geometry. M.Sc. thesis, Ludwig-Maximilians-Universität München, 2012.
- [15] Tukey, J. *The collected works of John W. Tukey*; Taylor & Francis, 1994; Vol. 1.
- [16] Milligen, B. V.; Sanchez, E.; Estrada, T.; Hidalgo, C.; Brañas, B.; Carreras, B.; Garcia, L. *Physics of Plasmas (1994-present)* **1995**, *2*, 3017–3032.
- [17] Milligen, B. V.; Hidalgo, C.; Sanchez, E.; Pedrosa, M.; Balbin, R.; Garcia-Cortés, I.; Tynan, G. *Review of scientific instruments* **1997**, *68*, 967–970.
- [18] Poli, F.; Lang, P.; Sharapov, S.; Alper, B.; Koslowski, H.; contributors, J.-E. *Nuclear Fusion* **2010**, *50*, 025004.
- [19] Manz, P.; Ramisch, M.; Stroth, U.; Naulin, V.; Scott, B. D. *Plasma Physics and Controlled Fusion* **2008**, *50*, 035008.
- [20] Manz, P.; Boom, J.; Wolfrum, E.; Birkenmeier, G.; Classen, I.; Jr, N. L.; Stroth, U. *Plasma Physics and Controlled Fusion* **2014**, *56*, 035010.
- [21] Smith, S. *The Scientist & Engineer's Guide to Digital Signal Processing*; California Technical Pub, 1997.
- [22] Wikimedia Commons, Window Function and Frequency Response - Hann on 2016.10.19. https://en.wikipedia.org/wiki/Window_function.
- [23] Schmid, A. Charakterisierung von Plasmafluktuationen mit einer kombinierten Mirnov-Langmuir-Sonde am Tokamak ASDEX Upgrade. M.Sc. thesis, Technische Universität München, 2005.

- [24] Mink, F.; Wolfrum, E.; Maraschek, M.; Zohm, H.; Horvth, L.; Laggner, F.; Manz, P.; Viezzer, E.; Stroth, U. *Plasma Physics and Controlled Fusion*, *accepted* **2016**,
- [25] Laggner, F. M. Inter - ELM pedestal evolution. 2016.
- [26] Mink, F. HEPP Presentation: Mode number determination from magnetic signals. 2015.
- [27] Diallo, A.; Groebner, R.; Rhodes, T.; Battaglia, D.; Smith, D.; Osborne, T.; Canik, J.; Guttenfelder, W.; Snyder, P. *Physics of Plasmas* **2015**, *22*.
- [28] Hatch, D.; Told, D.; Jenko, F.; Doerk, H.; Dunne, M.; Wolfrum, E.; Viezzer, E.; Team, T. A. U.; Pueschel, M. *Nuclear Fusion* **2015**, *55*, 063028.
- [29] Burckhart, A.; Wolfrum, E.; Fischer, R.; Lackner, K.; Zohm, H.; the ASDEX Upgrade Team, *Plasma Physics and Controlled Fusion* **2010**, *52*, 105010.
- [30] Ritz, C.; Powers, E.; Bengtson, R. *Physics of Fluids B: Plasma Physics (1989-1993)* **1989**, *1*, 153–163.
- [31] Kim, J.; Durst, R.; Fonck, R.; Fernandez, E.; Ware, A.; P.W.Terry, *Physics of Plasmas* **1996**, *3*, 3998–4009.